Physics of Fluids

RESEARCH ARTICLE | MARCH 10 2023

Influence of thermochemical nonequilibrium on expansion tube air test conditions: A numerical study

Special Collection: Hypersonic Flow

Sangdi Gu (顾桑迪) ; Jiaao Hao (郝佳傲) ; Qiu Wang (汪球) ; Chih-Yung Wen (温志湧)

Physics of Fluids 35, 036106 (2023)
https://doi.org/10.1063/5.0141281

Physics of Fluids ARTICLE scitation.org/journal/phf

Influence of thermochemical nonequilibrium on expansion tube air test conditions: A numerical study

Cite as: Phys. Fluids **35**, 036106 (2023); doi: 10.1063/5.0141281
Submitted: 4 January 2023 · Accepted: 21 February 2023 ·
Published Online: 10 March 2023

Sangdi Gu (顾桑迪),[1,a)] Jiaao Hao (郝佳傲),[1] Qiu Wang (汪球),[2] and Chih-Yung Wen (温志湧)[1]

AFFILIATIONS

[1]Department of Aeronautical and Aviation Engineering, The Hong Kong Polytechnic University, Kowloon, Hong Kong, China
[2]State Key Laboratory of High Temperature Gas Dynamics, Institute of Mechanics, Chinese Academy of Sciences, No. 15 Beisihuanxi Road, Beijing 100190, China

Note: This paper is part of the special topic, Hypersonic Flow.
[a)]**Author to whom correspondence should be addressed:** sangdi.gu@polyu.edu.hk

ABSTRACT

Using a Lagrangian solver, thermochemical nonequilibrium simulations are performed for the entire range of practical operating conditions of expansion tubes to isolate the influence of nonequilibrium and identify key features in large-scale facilities. Particular attention is given not only to the influence of the nonequilibrium unsteady expansion but also to the influences of the nonequilibrium region behind the primary shock and non-ideal secondary diaphragm rupture. The nonequilibrium unsteady expansion is found to be the most influential process in the test flow—it can significantly influence the flow properties and cause significant temporal variations in the properties during the test time. The nonequilibrium unsteady expansion is also found to accelerate the secondary shock and contact surface. The non-ideal secondary diaphragm rupture is found to increase the amount of nonequilibrium in the test flow due to the generation of a reflected shock. The nonequilibrium region behind the primary shock may be considered negligible in most conditions. Regarding the creation of thermochemical equilibrium test conditions, important factors for achieving this include having a high acceleration tube fill pressure, large-scale facility, and high total enthalpy. The combined effects of viscosity and nonequilibrium are postulated, and the results are supported by experimental works that report consistent findings. To provide an idea of the sensitivity of the numerical configuration, simulations of fixed-volume reactors at various de-excitation conditions are performed using different nonequilibrium models.

I. INTRODUCTION

Experimental hypersonic work is crucial for the development of hypersonic technology. An important type of wind tunnel used to facilitate this research is the expansion tube (ET), which can generate test conditions with a velocity greater than 15 km/s.[1] Figure 1 presents the schematic of a conventional *et al*ong with the position-time (x-t) diagram showing the major longitudinal wave processes that occur during the flow cycle. Upon rupture of the diaphragm (primary), separating the driver section and the shock tube (driven section), the driver gas (usually high-pressure and high-temperature helium) generates a propagating normal shock in the shock tube, which is filled with the test gas. This normal shock heats the test gas and then breaks a weak secondary diaphragm when it reaches the end of the shock tube. A one-dimensional (1D) unsteady expansion forms after the rupture of the secondary diaphragm. The shock-heated test gas travels through this unsteady expansion as it flows through the acceleration tube (which usually has the same cross-sectional area as the shock tube) before exiting into the test section. Ideally, the test time is defined as beginning with the passing of the secondary contact surface (CS) and ending with the arrival of the unsteady expansion.

One of the most important features of the ET flow cycle is the unsteady expansion of the test gas. Unlike steady expansions, unsteady expansions increase the total pressure and total enthalpy of test gas. This subsequently allows for extreme conditions to be generated in this facility. Also, with a very weak secondary diaphragm, stagnation of the test gas in the ET may be avoided, unlike most of the other hypersonic wind tunnels such as the reflected shock tunnel. This, together with the fact that part of the total enthalpy of the ET test condition is added via the unsteady expansion, means that this facility can generate a given total enthalpy test condition with less shock heating,

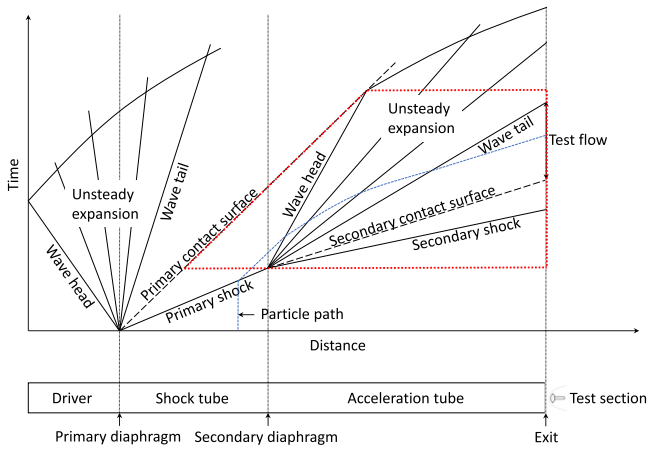

FIG. 1. Expansion tube and corresponding x-t diagram. The red dotted line bound the region simulated in this work.

which distorts and damages the test gas. As a result, the ET is useful not only for generating extremely high total pressure and/or total enthalpy conditions but also for generating better quality low enthalpy conditions.

Nevertheless, Ref. 2 suggests that a drawback of the ET is that "the thermodynamic state of the test flow cannot be accurately determined." The flow in ETs is complex and consists of processes—such as thermochemical nonequilibrium (NONEQ), turbulence, diaphragm rupture dynamics, boundary layer transition, acoustic disturbances, and the interactions between shock wave, contact surface, and boundary layer—that are still active areas of research. Without considering thermochemical nonequilibrium, a comprehensive study on the acoustic disturbances in ETs is reported in Ref. 3, and an exhaustive investigation of the interactions between shock wave, contact surface, and boundary layer in ETs is given in Ref. 4. An early recognition of the problem of thermochemical nonequilibrium in ETs is mentioned in Refs. 5 and 6, where an efficient numerical procedure was created for simulating the nonequilibrium unsteady expansion in ETs (which was essential at the time due to the undeveloped computational hardware). However, no subsequent application of this work to actually investigate nonequilibrium in ETs was ever made. Systematic and extensive research focusing on the nonequilibrium in ETs is still very much lacking. Hence, the current paper addresses this important need.

Thermochemical equilibrium (EQ) is often assumed for ET test conditions.[7] The physical argument for this is that because the acceleration tube can be relatively long (from a few meters to up to around 25 m for existing ETs) the flow should have enough time to reach equilibrium at the test section. However, there is scant evidence (both experimental and numerical) for this. Reference 8 used the measured shock speed in the acceleration tube to suggest that the test condition is close to equilibrium. However, as will be shown later in this paper, this way of gauging the thermochemistry in the test flow may not always be reliable. Also, thermochemical behavior is strongly dependent on the condition, but Ref. 8 tested only one condition ($u_\infty = 13$ km/s air, where u_∞ is the freestream velocity).

On the contrary, evidence of nonequilibrium in some ET test conditions has been reported. From Ref. 9, a numerical study on a $u_\infty \approx 4$ km/s air condition in the LENS-X ET (acceleration tube length = 26.5 m) showed the existence of vibrational nonequilibrium, which is known to influence experimental results.[10,11] Likewise, for similar air test conditions ($u_\infty \approx 3$–4 km/s) in this same facility, the numerical and experimental results reported in Ref. 12 gave indications that vibrational nonequilibrium may exist. Additionally, for a high enthalpy ($u_\infty \approx 8$ km/s) air test condition in the X3 ET (acceleration tube length = 24 m), the numerical study in Ref. 13 indicated significant chemical nonequilibrium.

In the current paper, using the numerical model described in Sec. II, thermochemical nonequilibrium simulations are performed for the entire range of practical operating conditions for ETs. Particular attention is given not only to the unsteady expansion from the secondary diaphragm rupture (Sec. III A) but also to the influences of the post-shock nonequilibrium before the unsteady expansion (Sec. III B) and non-ideal secondary diaphragm rupture process (Sec. III C). From these results, the combined effects of viscosity and nonequilibrium are postulated (Sec. IV A), and a discussion on generating equilibrium test conditions and flight test conditions is made (Sec. IV B). To provide an idea of the sensitivity of the finite-rate thermochemical kinetics model, simulations of fixed-volume reactors at various de-excitation conditions are performed using different models (Sec. V).

II. METHODOLOGY

The current work is carried out via 1D inviscid simulations with thermochemical nonequilibrium. As discussed in Refs. 2 and 14, the 1D inviscid approximation is valid for ETs with a high tube diameter to length ratio, such as the LENS-XX ET. Nevertheless, it is acknowledged that, in general, viscous effects can be important in ET flows. That said, the purpose of the current work is not necessarily to try to model the flow in ETs as accurately as possible. Instead, the current work aims to isolate the influence of nonequilibrium by using a 1D inviscid setup with nonequilibrium to identify key features. This is analogous to Ref. 4, which used a two-dimensional viscous setup assuming equilibrium to isolate the influence of the viscous effects to identify their key features.

As stated in Ref. 4, these ET simulations are computationally very expensive, which makes combining a two-dimensional viscous setup with a nonequilibrium model impractical, especially for the parametric analysis concerned in the current work. Instead, the combined effects of viscosity and nonequilibrium can be interpreted by consolidating the findings from the current work with those from Ref. 4 as done in Sec. IV A.

A. Numerical method

The current work is carried out using the open source L1d code, which is a 1D Lagrangian solver with second-order accuracy in both space and time combined with a robust shock-capturing scheme.[15,16] It is an explicit code that calculates the time evolution of internal wave and flow processes in hypersonic impulse facilities. In the code, the facility is divided into gas slugs. The slugs are discretized, axially, into fixed-mass cells as shown in Fig. 2, which move along the tube. According to the Lagrangian description,

$$\frac{dx_{j\pm\frac{1}{2}}}{dt} = u_{j\pm\frac{1}{2}}, \tag{1}$$

where x is the position of the interface, and u is the local gas velocity determined with the Riemann solver described in Ref. 17. The average density in the cell, $\overline{\rho_j}$, is

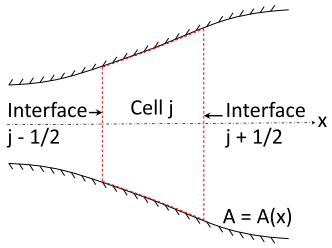

FIG. 2. A control-mass (Lagrangian cell). Adapted from Ref. 15.

$$\overline{\rho_j} = \frac{m_j}{\overline{A_j}\left(x_{j+\frac{1}{2}} - x_{j-\frac{1}{2}}\right)}, \tag{2}$$

where $\overline{(\ldots)}$ represents a cell average, A is the duct area and m_j is the (constant) mass of gas in cell j. Assuming an inviscid condition, the pressure forces acting on the cell interfaces cause a momentum change in the cell, as given by

$$\frac{dm_j\overline{u_j}}{dt} = p_{j-\frac{1}{2}}A_{j-\frac{1}{2}} - p_{j+\frac{1}{2}}A_{j+\frac{1}{2}} + \overline{p_j}\left(A_{j+\frac{1}{2}} - A_{j-\frac{1}{2}}\right). \tag{3}$$

Assuming an adiabatic condition, the work done at the cell interfaces causes an energy change in the cell, as given by

$$\frac{dm_j\overline{E_j}}{dt} = p_{j-\frac{1}{2}}A_{j-\frac{1}{2}}u_{j-\frac{1}{2}} - p_{j+\frac{1}{2}}A_{j+\frac{1}{2}}u_{j+\frac{1}{2}}, \tag{4}$$

where E is the total specific energy. Although L1d can accommodate area changes as shown in the above-mentioned equations, this feature is unused for the current work, which only deals with constant-area ducts.

Park's 2T model,[18] where molecules are destroyed/created at the average vibrational energy and dissociation/recombination reactions are controlled by $T_c = T_{tr}^{0.5}T_v^{0.5}$, with T_{tr} and T_v being the translational-rotational and vibrational temperatures, respectively, is used to describe the thermochemical nonequilibrium. The translational temperature is the temperature giving the translational energy component of the internal energy, and, likewise, for the rotational and vibrational temperatures. In the 2T model, the translational and rotational temperatures are assumed equal (T_{tr}) because only a few molecular collisions are typically needed to equilibrate the rotational and translational modes.[19] The molecular vibrational energy conservation equation for a Lagrangian cell is

$$\frac{d\overline{e_v}}{dt} = \frac{1}{\overline{\rho_j}}\left(\sum_{i=N_2,O_2,NO}\overline{\rho_{j,i}}\frac{\overline{e_{v,i}^{eq}} - \overline{e_{v,i}}}{\overline{\tau_{v,i}}} + \overline{e_{v,i}}\,\overline{\dot{w}_i}\right), \tag{5}$$

where e_v and $e_{v,i}$ are the specific vibrational energies of the mixture and species i (molecules only), respectively; $\dot{w}_i$ and $\tau_{v,i}$ is the mass production rate and the vibrational relaxation time of i, respectively—both calculated according to Park's 2T model;[18] and $\rho_{j,i}$ is the density of i. Similarly, the species conservation equation for a Lagrangian cell is

$$\frac{d\overline{c_i}}{dt} = \frac{\overline{\dot{w}_i}}{\overline{\rho_j}}, \tag{6}$$

where c_i is the mass fraction of species i (atoms and molecules).

Time advancement is carried out using the predictor-corrector scheme. Further details on the description of the L1d code and its usage can be found in Refs. 15 and 16. As will be demonstrated in this paper, the Lagrangian simulation allows for many interesting and useful analyses, which may otherwise be difficult to carry out via Eulerian simulations.

B. Validation study

L1d has been comprehensively validated via experimental and theoretical means for simulating the transient flow in hypersonic impulse facilities including shock tubes,[16] reflected shock tunnel,[15,20,21] ETs,[22] and gun tunnels.[23,24] Moreover, the numerical model of L1d has been independently implemented in Refs. 12 and 14 in their *Jaguar* code and further validated experimentally and theoretically for ETs. The reader is referred to these papers for details of these validations. In the current paper, we will present the classic test case of Sod's shock tube[25] to demonstrate the basic performance of the code—the extreme test case of LeBlanc's shock tube[25] to demonstrate the code's ability at simulating strong shocks and expansions and the well-established test case of Grossman and Cinnella's shock tube[26] to demonstrate the code's capability at simulating high-enthalpy nonequilibrium conditions.

Using an initial uniform spatial discretization of 5 mm in each slug (no clustering) and a Courant–Friedrichs–Lewy (CFL) number of 0.5, Sod's shock tube is simulated in L1d, and the result is compared with the analytical solution as shown in Fig. 3. A good agreement is observed. The shock is captured in 3–4 cells and has the correct speed. Typical for a Lagrangian scheme, as discussed in Refs. 16, 27, and 28, there exists a small glitch at the contact discontinuity on the driven (test) gas side due to the starting error. The edges of the expansion fan and contact surface show some smearing but can be sharpened without increasing the total number of cells by clustering the initial spatial discretization of the driver gas slug toward the contact surface. The result is shown in Fig. 3 for clustering the driver gas cells in this way to an initial minimum cell size of 1.5 mm while still using a CFL number of 0.5.

LeBlanc's shock tube,[25] which is a notoriously difficult calorically perfect gas ($\gamma = 1.4$) test case with initial pressure and temperature ratios of 10^9:1 and 10^6:1, respectively, is simulated in L1d using an initial uniform spatial discretization of 10 mm in the driven gas slug, an initial minimum cell size of 0.3 mm in the driver gas slug with clustering toward the contact surface, and a CFL number of 0.5. The results are shown in Fig. 4, and one can see that L1d simulates the extremely strong shock and expansion accurately even in this brutal problem.

Grossman and Cinnella's shock tube,[26] which consists of a driver section filled with a dissociated air mixture initially at equilibrium at a temperature of 9000 K and a pressure of 195 256 Pa and a driven section filled with air at 300 K and 10 000 Pa, is simulated in L1d using the nonequilibrium model described in Sec. II A. Using an initial uniform spatial discretization of 0.36 mm in the driven gas slug, an initial minimum cell size of 90 μm in the driver gas slug with clustering toward the contact surface, and a CFL number of 0.5, the L1d result is shown in Fig. 5. Because Grossman and Cinnella's shock tube does not have an exact theoretical solution, the L1d result is compared with several other numerical solutions obtained independently using different codes. A good agreement is seen for all parameters—the L1d result falls within the range of the other solutions.

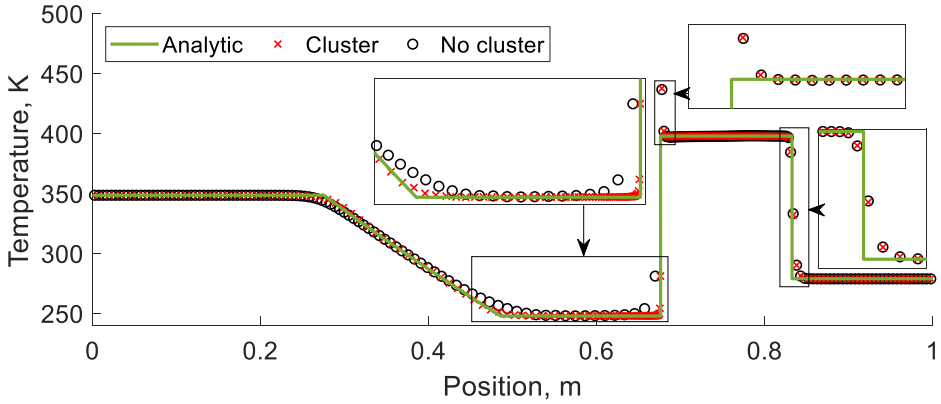

FIG. 3. Temperature distribution in Sod's shock tube problem at $t = 0.6$ ms.

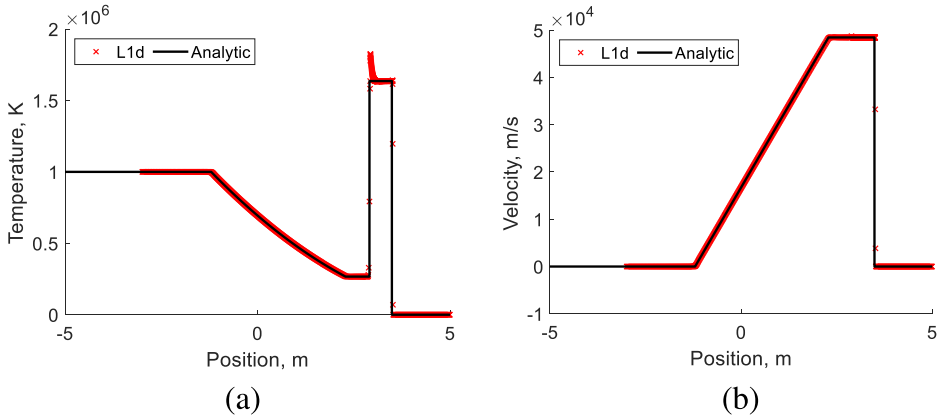

FIG. 4. (a) Temperature and (b) velocity distribution in LeBlanc's shock tube problem at $t = 60$ μs.

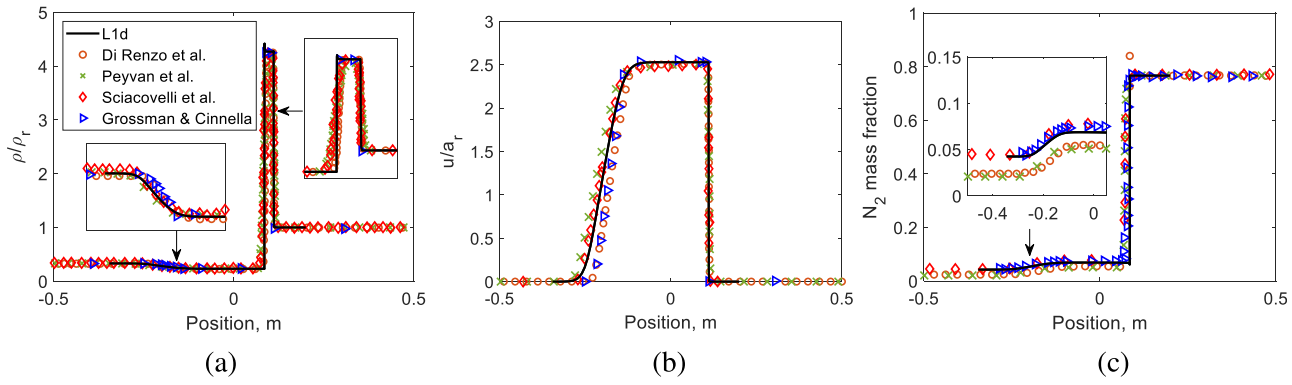

FIG. 5. (a) Density, (b) velocity, and (c) N_2 mass fraction in Grossman and Cinnella's shock tube at the moment when the shock has traveled 0.11 m in the shock tube. The subscript "r" refers to the initial condition in the driven tube. Along with the L1d result, the solutions from Grossman and Cinnella,[26] Di Renzo *et al.*,[29] Peyvan *et al.*,[30] and Sciacovelli *et al.*[31] are shown.

C. Computational domain and simulation setup

An example of the L1d computational domain and simulation setup for the current work is shown in Fig. 6. The region in the ET x-t diagram, which is simulated, is illustrated in Fig. 1 (red dotted line). The simulation only considers the test and accelerator gases and does not consider the entire ET flow cycle. Preserving generality, the driver is not considered due to the numerous techniques available to drive the same test condition.[1] The initial state of the simulation is at the moment when the primary shock reaches the secondary diaphragm. Therefore, the initial condition of the test gas slug is the post-shock

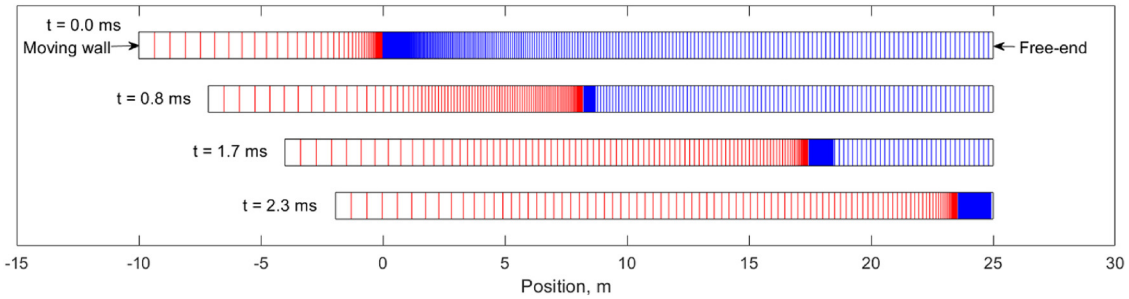

FIG. 6. L1d computational domain and Lagrangian cells for the test gas slug (red) and acceleration gas slug (blue). For clarity in the figure, the resolution is reduced by factors of 2 and 20 in the test gas and accelerator gas slugs, respectively.

condition. The primary contact surface (interface between the driver gas and test gas) is modeled as a moving wall traveling at a velocity equal to the post-shock velocity. The initial condition of the accelerator gas slug is the fill condition. The right boundary of the accelerator gas slug is a free-end, which is a supersonic (extrapolated) outflow. Between the test and accelerator gas slugs exists a gas–gas interface. The reader is referred to Ref. 16 for further details on the numerical implementation of these boundary conditions.

The thermochemistry of the test gas slug is described by a five species—N_2, O_2, N, O, NO—nonequilibrium air (N_2:0.78, O_2:0.22 mole fractions) model. This is valid for simulating ET conditions as the test gas is usually not shocked hard enough to produce any significant ionization. The thermochemistry of the accelerator gas slug is described by the equilibrium air model of NASA's CEA (Chemical Equilibrium with Applications), including ions (25 species). Nonequilibrium in the accelerator gas does not need to be described here because the shock-processed accelerator gas is dominated by equilibrium flow and the nonequilibrium post-shock region is too small to have any significant influence on ET test conditions, especially for large-scale facilities.[32] Nevertheless, ions are required to be modeled here as the secondary shock speed in ETs is commonly high enough to cause significant ionization of the accelerator gas.

At present, large-scale facilities are the subject of significant interest, which is expected to further increase in the future.[33–35] Thus, the accelerator gas slug is initially 25 m long to model a 25 m acceleration tube corresponding to a large-scale ET like the LENS XX and X3.[9,22] The initial length of the test gas slug is 10 m, which is long enough to prevent the unsteady expansion fan head from reaching the moving wall during the time scales considered for the current work. Subsequently, the test times observed will correspond to the maximum ET test time where termination is caused by the arrival of the unsteady expansion fan tail as shown in Fig. 1.

Because this is a Lagrangian simulation, the spatial locations of the cells are not fixed; Fig. 6 shows the movement of the cells as time advances. The test gas slug gets stretched, while the acceleration gas slug gets compressed, which is expected as the test gas undergoes expansion, while the acceleration gas undergoes shock compression. Strong clustering is used in the test gas slug for a better solution as mentioned in Sec. II B, while mild clustering is used in the accelerator gas slug for the robustness of the computation during the start of the simulation.

III. RESULTS

Nonequilibrium simulations are performed for the entire range of practical operating conditions for ETs that corresponds to primary shock speeds of 2–7 km/s, shock tube fill pressures of 1–100 kPa, and acceleration tube fill pressures of 1–100 Pa.[1,36,37] As shown in Table I, 12 test conditions are selected to cover this range of conditions. Conditions 1–6 correspond to the high shock tube fill pressure conditions, while conditions 7–12 correspond to the low shock tube fill pressure conditions. The odd-numbered conditions correspond to the low acceleration tube fill pressure conditions, while the even-numbered conditions correspond to the high acceleration tube fill pressure conditions. Primary shock speeds of 2, 4, and 7 km/s are tested. The resulting computed thermochemical state of the test conditions (for a 25 m acceleration tube) is also summarized in Table I, while detailed discussions of the results for each condition are presented herein in the subsequent sections.

TABLE I. Simulated ET test conditions. Thermal nonequilibrium, chemical nonequilibrium, thermal equilibrium, and chemical equilibrium are referred to as "TNE," "CNE," "TE," and "CE," respectively.

Condition	1	2	3	4	5	6	7	8	9	10	11	12
Primary shock speed (km/s)	2	2	4	4	7	7	2	2	4	4	7	7
Shock tube fill pressure (kPa)	100	100	100	100	100	100	1	1	1	1	1	1
Acceleration tube fill pressure (Pa)	1	100	1	100	1	100	1	100	1	100	1	100
Test condition thermochemical state	TNE	TNE	TNE, CNE	TE, CNE	TNE, CNE	TE, CE	TNE	TE	TNE, CNE	TE, CE	TNE, CNE	TE, CE

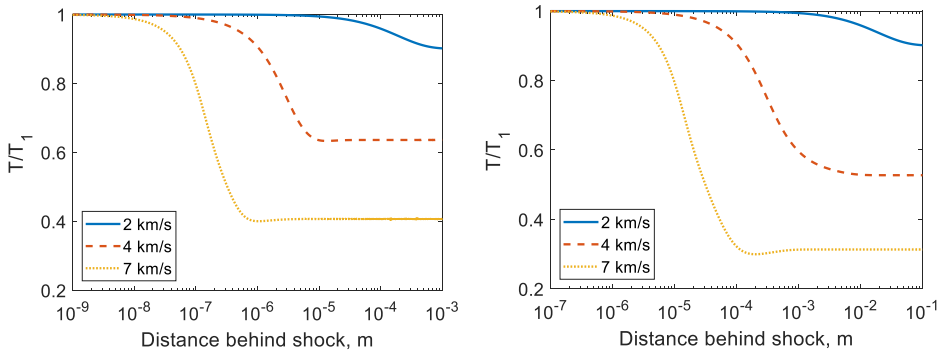

FIG. 7. Normalized post-shock temperature profile for shock tube fill pressures of (a) 100 kPa and (b) 1 kPa calculated using the space-marching code POSHAX[32] with Park's 2T model. T_1 is the frozen temperature immediately downstream of the shock front.

Reference 2 recognized that the test flow in ETs "undergoes a dual nonequilibrium process, first behind the primary shock and second in the expansion process. This causes difficulty in determining the state of the gas in the test section." The post-shock nonequilibrium in the shock tube is often ignored in previous studies, and the equilibrium post-shock state is usually the initial condition of the unsteady expansion.[5,6,38–42] The basis for this assumption is that the post-shock relaxation distance may be short enough such that the slug of test gas in the test flow mostly originates from the equilibrium post-shock region. This could be true when a high shock tube fill pressure is used; as shown in Fig. 7(a) for a fill pressure of 100 kPa, the post-shock relaxation distance is less than 1 mm even for shock speeds as low as 2 km/s. However, when using a low shock tube fill pressure, the relaxation distance is about two orders of magnitude longer as shown in Fig. 7(b) for a fill pressure of 1 kPa. In this case, the post-shock nonequilibrium may be important for correctly describing the thermochemistry of the test condition; this is analyzed in Sec. III B.

A. Unsteady expansion nonequilibrium (conditions 1–6)

In this section, results for conditions 1–6 are presented. For these conditions, a uniform equilibrium post-shock condition is used as the pre-expansion condition, and the subsequent analysis focus on the thermochemistry from the unsteady expansion. Nominally, in these simulations, 200 and 5000 cells are used for the test gas and accelerator gas slugs, respectively, with the minimum cell length being 3 and 900 μm for the test gas and accelerator gas slugs, respectively. A nominal value of 0.5 is used for the CFL number. Confirmation of adequate convergence of both spatial and temporal discretization is made by testing with a finer mesh (2× nominal) and with a smaller CFL number (0.25), using condition 5. The results for the temperature, which is sensitive to both gasdynamic and thermochemical processes, are shown in Fig. 8. Not only does the temperature of the three results essentially show no differences but the location of the shock and contact surface at $t = 1.16$ ms from the three results are also matched. Since the nominal spatial and temporal discretization achieves this for condition 5, which is the highest primary shock speed condition expanding into the lowest acceleration tube fill pressure resulting in the largest gradients in flow properties, spatial and temporal convergence is expected for the other conditions (within conditions 1–6) too when using the nominal setup.

1. Low acceleration tube fill pressure (conditions 1, 3, and 5)

The temporal results of the temperatures and static pressure at a fixed spatial location of 25 m in the acceleration tube are shown in Fig. 9 for conditions 1, 3, and 5; this would be the flow experienced by the test model if it is placed at this location. Defining the test time as beginning with the passing of the contact surface and ending with the arrival of the unsteady expansion as shown in Fig. 1; the test time is labeled. The test time is not steady. In Fig. 1, only the major wave processes are indicated. Under ideal conditions (inviscid and perfect gas or equilibrium), the flow properties in the test time would be completely steady. However in reality, viscous effects and nonequilibrium can generate wave processes that cause nonuniformities in the slug of test flow resulting in significantly unsteady test flows. The current work examines the influence of nonequilibrium.

From Fig. 9, the static pressure and translational temperature both increase during the test time in all three conditions. The vibrational temperature is mostly in nonequilibrium and decreases during the test time. To further examine this nonequilibrium caused by the unsteady expansion, the temperature history of two Lagrangian cells, L_1 and L_2, in each condition is extracted and shown in Fig. 10. L_1 and L_2 are roughly selected cells for each condition that approximately bound the downstream and upstream ends, respectively, of the portion of test gas making up the test time at 25 m in the acceleration tube. That is, L_1 is some cell that arrives at the test section (25 m downstream in the acceleration tube) near the beginning of the test time, and L_2 is some cell that arrives near the end.

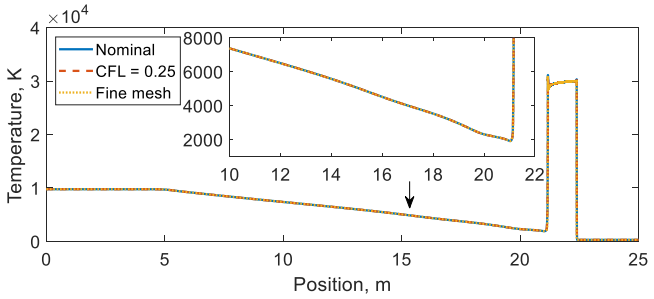

FIG. 8. Translational temperature distribution for condition 5 at $t = 1.16$ ms.

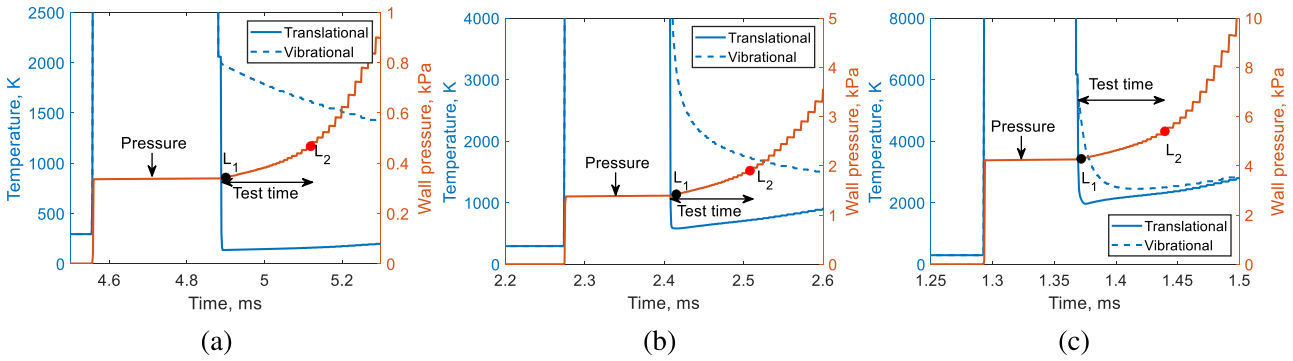

FIG. 9. Temperatures and static pressure for conditions (a) 1, (b) 3, and (c) 5. All at 25 m in the acceleration tube.

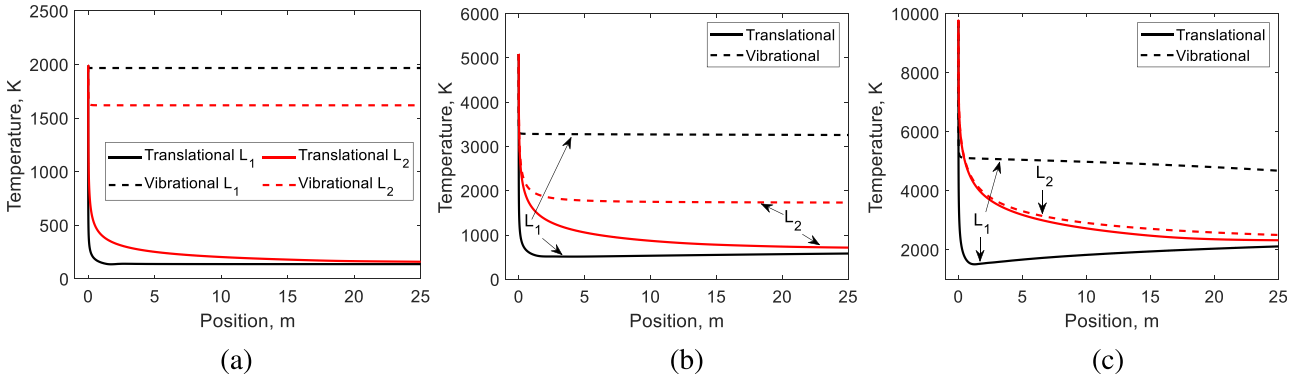

FIG. 10. Temperatures history of Lagrangian cells L_1 and L_2 in conditions (a) 1, (b) 3, and (c) 5.

Qualitatively illustrated in Fig. 11, L_1 undergoes a more rapid expansion compared to L_2 and, thus, would be more frozen (FR) than L_2. This behavior is quantitively evident in Fig. 10, which shows that L_2 has a lower vibrational temperature than L_1 at 25 m in all three conditions. Also, Fig. 10 shows that the vibrational mode of L_1 remains almost frozen after traversing the expansion fan and no noticeable equilibration occurs as it travels downstream in the acceleration tube after the expansion. This is an interesting result because a possible mechanism for having equilibrium ET test conditions is equilibration after the unsteady expansion; the result shows that this is not possible for conditions 1, 3, and 5, as well as the other conditions tested in this work, at the current length scale. This finding is consistent with the numerical results in Refs. 5 and 6.

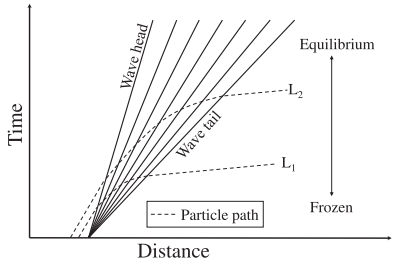

FIG. 11. A 1D centered unsteady expansion fan shown qualitatively in an x-t diagram.

For conditions 3 and 5, because the pre-expansion temperature is high enough for dissociation of the molecules, nonequilibrium not only occurs in the vibrational modes but occurs also in the chemical modes (unlike condition 1 that contains only vibrational excitation). In condition 3, the pre-expansion temperature is high enough for significant dissociation of O_2, but not N_2. In condition 5, the pre-expansion temperature is high enough for significant dissociation of both O_2 and N_2. The mass fraction results for conditions 3 and 5 are shown in Fig. 12. Throughout the test time, significant nonequilibrium is observed in the O_2 mass fraction, which continuously increases, in both conditions. On the other hand, the N_2 mass fraction is steady and in equilibrium throughout the test time in condition 5. In Fig. 12, and in all subsequent mass fraction results presented in this paper, the equilibrium mass fraction refers to the equilibrium mass fraction at the instantaneous local static pressure and translational temperature. That is, the equilibrium mass fractions shown in Fig. 12 correspond to those at the static pressure and translational temperature shown in Fig. 9. The difference between the equilibrium and nonequilibrium mass fractions then gives a clear and direct indicator of the amount of nonequilibrium in the mass fractions relative to the local condition.

Looking at the O_2 mass fraction history of the two Lagrangian cells, L_1 and L_2, as shown in Fig. 13, for conditions 3 and 5, the

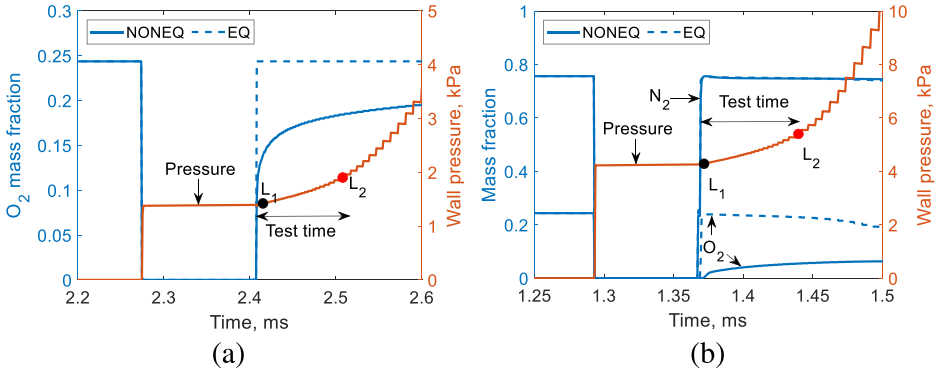

FIG. 12. Mass fractions and static pressure for conditions (a) 3 and (b) 5. All at 25 m in the acceleration tube.

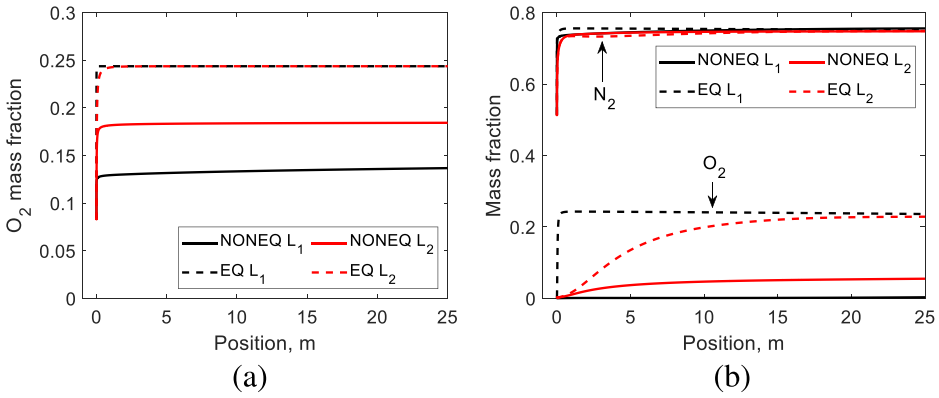

FIG. 13. Mass fraction history of Lagrangian cells L_1 and L_2 in conditions (a) 3 and (b) 5.

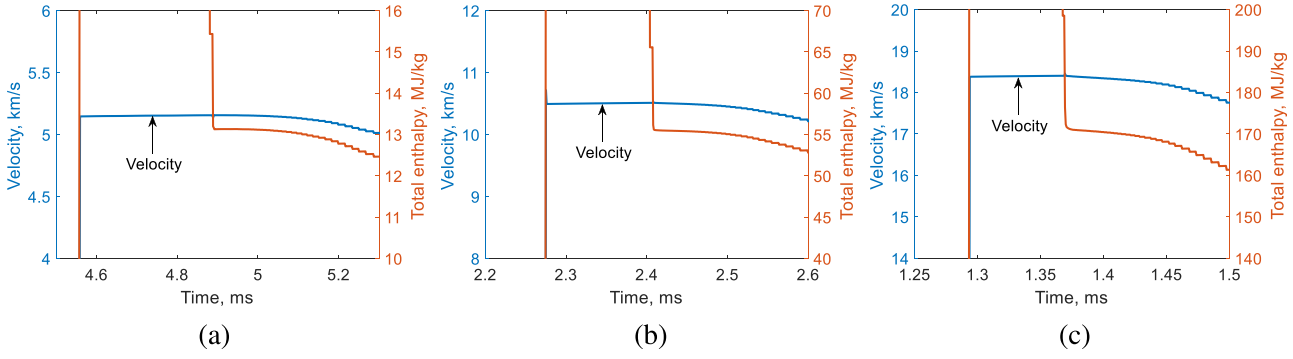

FIG. 14. Velocity and total enthalpy for conditions (a) 1, (b) 3, and (c) 5. All at 25 m in the acceleration tube.

behavior is qualitatively the same as that for the temperatures (Fig. 10)—L_1 has greater nonequilibrium than L_2 at 25 m, and the mass fraction of L_1 essentially freezes after the expansion (there is only some minor equilibration occurring in L_1 after the expansion). On the other hand, the N_2 mass fraction is essentially equilibrated in both L_1 and L_2 in condition 5.

As a result of the significant variation in temperatures, static pressure, and mass fraction during the test time, as shown in Figs. 9 and 12, the other flow properties including the density, pitot pressure, Mach number, and unit Reynolds number change appreciably during the test time too. The exceptions are the velocity and total enthalpy, which remain relatively constant during the test time as shown in Fig. 14; this is a general result seen not only in conditions 1, 3, and 5 but in all the conditions tested in the current work. The result for the total enthalpy is interesting because an important differentiating characteristic between a steady expansion and an unsteady expansion is that the total enthalpy remains constant and is independent of the thermochemistry in the former, while the total enthalpy changes and is dependent on the thermochemistry in the later. The current result shows that, despite the thermochemical state (vibrational temperature

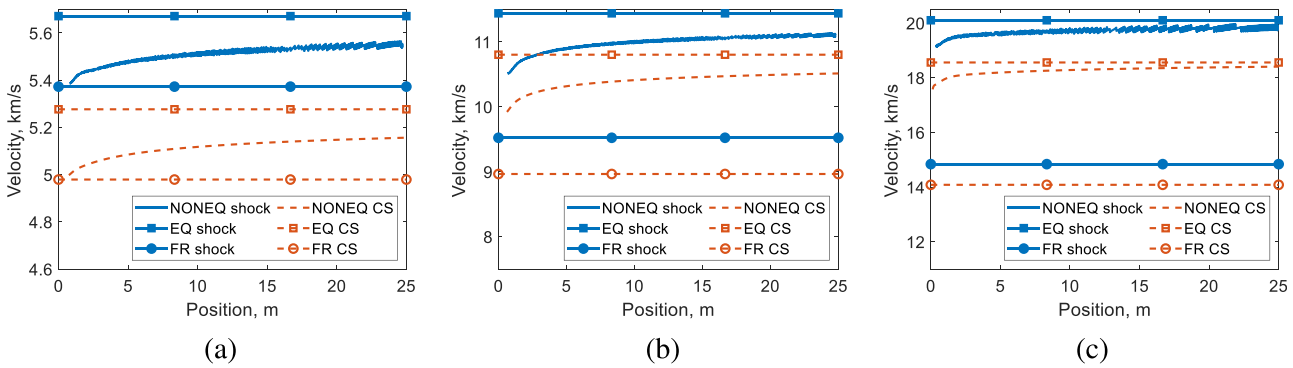

FIG. 15. Nonequilibrium (NONEQ) secondary shock and secondary contact surface (CS) speeds along with the frozen (FR) and equilibrium (EQ) limits for conditions (a) 1, (b) 3, and (c) 5.

and mass fractions) changing significantly during the test time in the ET, the total enthalpy can remain essentially steady for practical intents and purposes.

Another important aspect examined is the secondary shock speed, which is an easily measurable parameter in experiments and is influenced by the thermochemistry in the unsteady expansion. The results are shown in Fig. 15 along with the theoretical frozen and equilibrium limits. These limits are obtained, using the method in Ref. 43, by iteratively solving the secondary shock speed, which gives constant velocity and static pressure across the secondary contact surface, assuming frozen and equilibrium unsteady expansions. The nonequilibrium shock speed (and contact surface) starts near the frozen limit and accelerates toward the equilibrium limit in all three conditions. The pressure gradient seen in Fig. 9 during the test time in these conditions drives this acceleration. The shock is driven by the contact surface, which is in turn driven by the unsteady expansion. Nevertheless, the magnitude of the acceleration is not large enough to produce any significant gradient in the test flow velocity as shown in Fig. 14; this is a general result seen in all the conditions tested in the current work.

Looking at the thermochemistry inside the unsteady expansion fan, as shown exemplarily in Fig. 16 for condition 1, the distance between the expansion wave head and expansion wave tail increases with increasing time, and the flow inside the expansion fan tends toward equilibrium as the secondary shock propagates downstream. As a result, the shock speed tends toward the equilibrium limit as it propagates downstream. Because the shock speed is dependent on the thermochemistry of the flow inside the expansion fan rather than the thermochemistry of the expanded flow outside the expansion fan, the shock speed may not be a reliable indicator for the degree of nonequilibrium in the test flow. That is, one might find for certain conditions at a certain distance downstream in the acceleration tube a shock speed that is close to equilibrium but a test flow with significant nonequilibrium, because the flow can remain frozen after traversing the expansion fan. This is exemplified in condition 5 at 25 m downstream in the acceleration tube where the shock speed is relatively near the equilibrium value as shown in (c), but the test flow contains appreciable nonequilibrium in the O_2 mass fraction as shown in Fig. 12(b).

2. High acceleration tube fill pressure (conditions 2, 4, and 6)

The results for conditions 2, 4, and 6 are shown in Figs. 17 and 18 at 25 m in the acceleration tube. As these conditions have a higher acceleration tube fill pressure compared to conditions 1, 3, and 5 presented in Sec. III A 1 (100 Pa compared to 1 Pa), the test gas is, therefore, subjected to a weaker expansion, which means that the test flows should be closer to thermochemical equilibrium. This is indeed the case when examining the results. Condition 2 is rather steady with some mild thermal nonequilibrium. Condition 4 is rather steady and in thermal equilibrium with some mild chemical nonequilibrium. When examining the Lagrangian cells in conditions 2 and 4, it is found that any thermochemical relaxation achieved occurs essentially entirely during (not after) the unsteady expansion, which is consistent with the earlier findings in Sec. III A 1. Condition 6 is very steady and

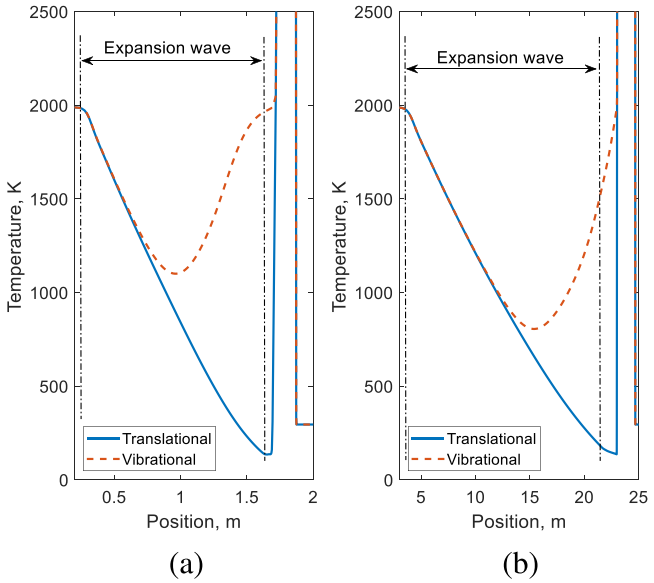

FIG. 16. Condition1 temperature distribution at (a) $t = 0.34$ and (b) $t = 4.5$ ms.

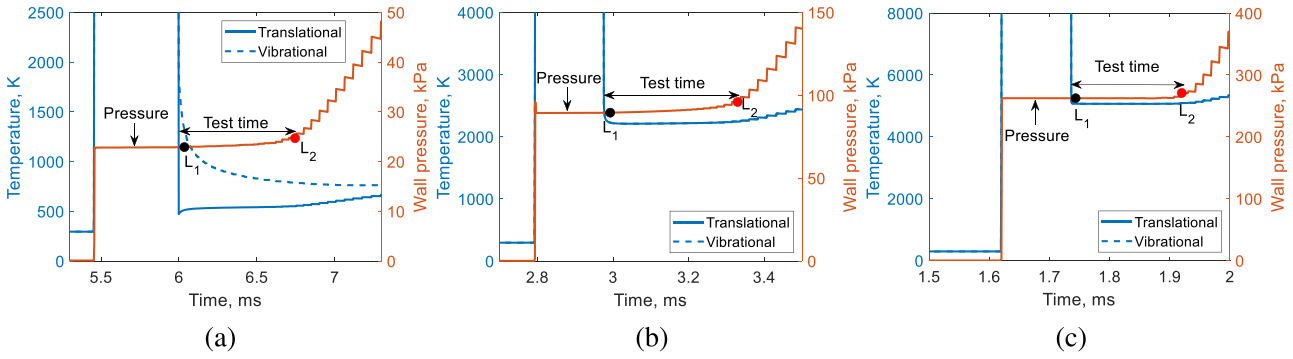

FIG. 17. Temperatures and static pressure for conditions (a) 2, (b) 4, and (c) 6. All at 25 m in the acceleration tube.

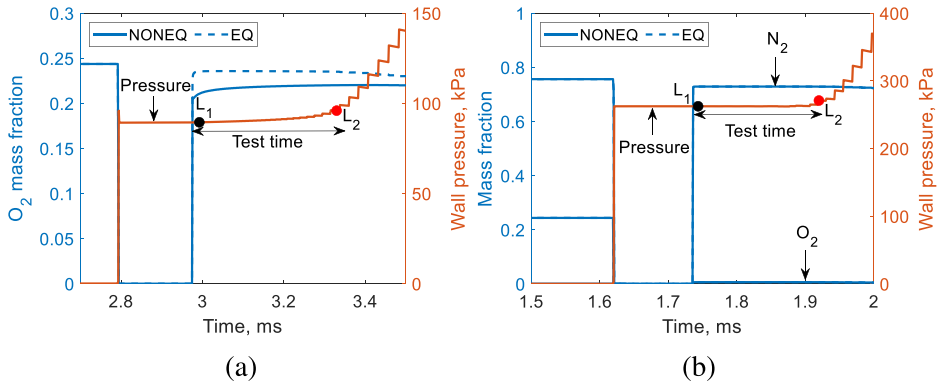

FIG. 18. Mass fractions and static pressure for conditions (a) 4 and (b) 6. All at 25 m in the acceleration tube.

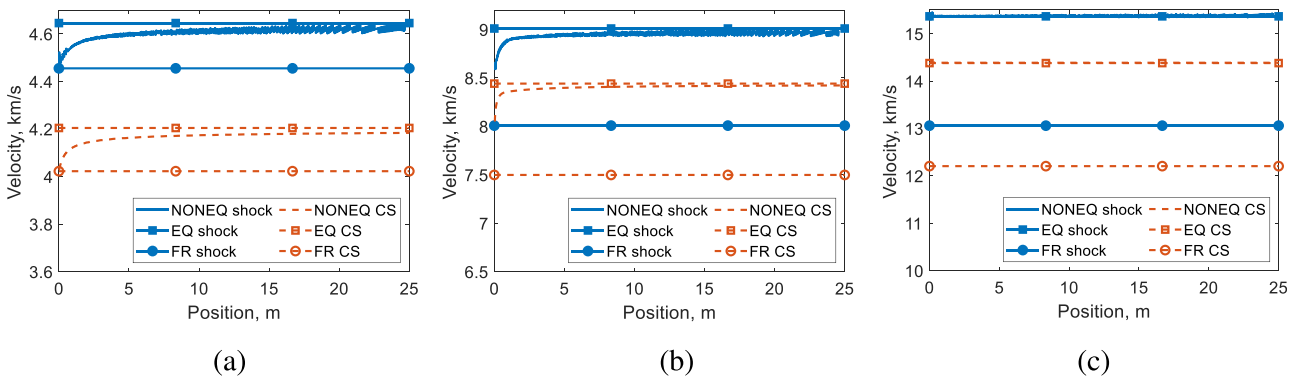

FIG. 19. Nonequilibrium (NONEQ) secondary shock and secondary contact surface (CS) speeds along with the frozen (FR) and equilibrium (EQ) limits for conditions (a) 2, (b) 4, and (c) 6.

entirely equilibrated, and the Lagrangian cells are in thermochemical equilibrium throughout their trajectory.

The better equilibration of conditions 2, 4, and 6, compared with conditions 1, 3, and 5, is also evident in the secondary shock and secondary contact surface speeds; as shown in Fig. 19, the shock and contact surface speeds in conditions 2, 4, and 6 reach near the equilibrium limit at 25 m. The shock speeds are essentially not accelerating by 25 m, and this result is reflected in the static pressures shown in Fig. 17, which is quite steady with little pressure gradient. To better illustrate the role of the pressure gradient in accelerating the shock wave, Fig. 20 is created exemplarily using condition 2. The spatial distribution of the static pressure is shown at three different moments in time that corresponds to the shock being at the 2 m, 13 m, and 24 m locations. The spatial locations are shifted such that the contact surface is located at 0 m in all cases. There exists a pressure gradient in the test gas outside of the expansion fan. This pressure gradient increases the

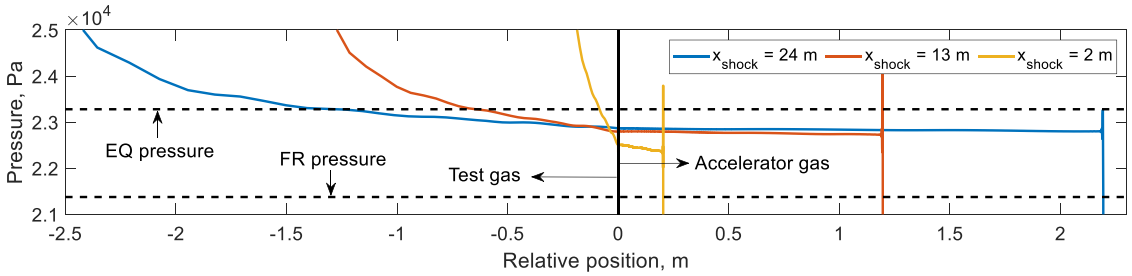

FIG. 20. Condition 2 NONEQ spatial distribution of the static pressure for different locations of the shock, x_{shock}, and the EQ and FR pressure limits corresponding to the EQ and FR shock/CS speed limits.

pressure of the accelerator gas, which in turn increases the shock speed. The gradient is strong when the shock has a large acceleration and vice versa. For example, at $x_{shock} = 2$ m, the gradient is so strong it is difficult to identify the arrival of the expansion fan. The gradient is caused by the equilibration of the flow inside the expansion fan. As shown in Fig. 20, the equilibrium pressure is the upper bound, and the frozen pressure is the lower bound. Therefore, the gradual equilibration of the flow inside the expansion fan causes a constant increase in the post-expansion pressure, which in turn increases the shock speed.

Due to the increase in shock speed and the necessary condition that the static pressure across the contact surface is constant, the static pressure cannot really retain information about its past—the same can be said for the velocity. This is unlike the mass fractions and the translational and vibrational temperatures, which can retain histories of their nonequilibrium past and can remain largely frozen after the expansion. Hence, the shock speed and static (wall) pressure—the two most easily measured properties of an ET test condition—may not be reliable indicators for the degree of nonequilibrium in the test condition.

Comparing conditions 2, 4, and 6 in Fig. 19, it can be observed that greater equilibration occurs with increasing total enthalpy of the conditions. Looking at the shock and contact surface speeds in Fig. 19(b) for condition 4, it is qualitatively similar to those of condition 2 except with indications of more equilibration. The shock and contact surface speeds for condition 4 accelerate rapidly in the beginning and reach near the equilibrium limit after only around 3 m, which is much earlier than that in condition 2. Moreover, looking at Fig. 19(c) for condition 6, the shock and contact surface speeds are at the equilibrium limit throughout. This trend of greater equilibration with increasing total enthalpy is consistent with the results in Ref. 44 for nozzle flows that showed that more equilibration occurs in the higher enthalpy conditions due to the higher translational temperatures involved in the flow, which produces faster thermochemical reaction rates, which promotes greater thermochemical relaxation. For nonequilibrium unsteady expansions, the higher temperature and pressure involved in the higher enthalpy conditions promote equilibration and outweigh the higher velocities (shorter time scales) involved in these conditions, which promote thermochemical freezing. This same trend can also be observed in the results from Sec. III A 1 when examining the nonequilibrium shock and contact surface speeds relative to the EQ and FR limits among conditions 1, 3, and 5 shown in Fig. 15. Furthermore, this explains why equilibrium shock speeds were experimentally measured in a small-scale facility (acceleration tube length = 1.3 m) in Ref. 8, where a 108 MJ/kg (very high-enthalpy, u_∞=13 km/s) condition was tested.

3. Significance of the post-shock nonequilibrium region

As mentioned earlier, when modeling ET flows, the flow in the shock tube has generally been assumed to be in thermochemical equilibrium.[5,6,38–42] This could be true when a high shock tube fill pressure is used like in conditions 1–6; as shown in Fig. 7(a) for a fill pressure of 100 kPa, the post-shock relaxation distance is less than 1 mm for shock speeds as low as 2 km/s. To assess the validity of assuming a uniform equilibrium post-shock condition, an analysis of the Lagrangian cells is performed to determine the portion of the test gas in the shock tube corresponding to the test flow. The results are shown in Table II along with the post-shock relaxation distance extracted from Fig. 7(a). The results show that, apart from condition 1, the test flow at 25 m for all conditions originates from a portion of the test gas in the shock tube, which is at least an order of magnitude larger than the post-shock relaxation distance. This means that the nonequilibrium post-shock portion of the test gas would contribute to only a small portion of the test flow in these cases, which suggests that the simplification to a uniform equilibrium post-shock condition for the pre-expansion condition would be valid in most cases.

As shown in Table II, the validity of assuming a uniform equilibrium post-shock condition for the pre-expansion condition is enhanced for higher enthalpy test conditions where the post-shock relaxation distance is smaller, and for higher acceleration tube fill

TABLE II. The post-shock relaxation distance of the shock in the shock tube and the length of the portion of the test gas in the shock tube corresponding to the test flow for conditions 1–6 for a 25 m acceleration tube.

Condition	1	2	3	4	5	6
Post-shock relaxation distance (m)	1×10^{-3}	1×10^{-3}	1×10^{-5}	1×10^{-5}	1×10^{-6}	1×10^{-6}
Portion of test gas in shock tube (m)	2×10^{-3}	7×10^{-2}	8×10^{-4}	4×10^{-2}	6×10^{-4}	3×10^{-2}

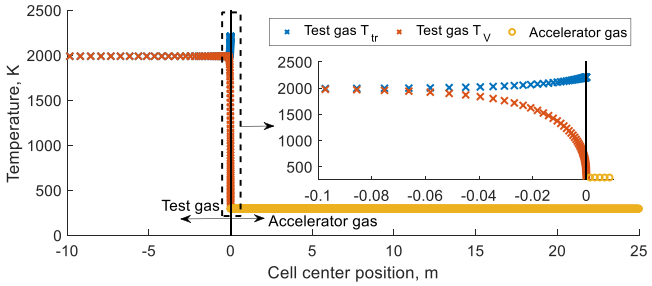

FIG. 21. Initial temperature distribution and cell center positions for conditions 7 and 8. For clarity in the figure, only every second point is shown.

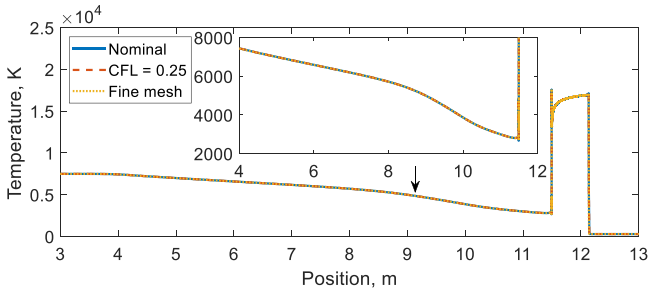

FIG. 22. Translational temperature distribution for condition 11 at $t = 0.85$ ms.

pressure conditions where the test gas is less expanded, resulting in the test flow originating from a longer portion of the test gas in the shock tube. The validity of the assumption also depends on the length of the acceleration tube. The results currently shown correspond to a 25 m acceleration tube. As the length of the acceleration tube decreases, the length of the portion of the test gas in the shock tube from which the test flow originates also decreases. The current study revealed that the relationship is basically linear. So, for a small-scale facility with an acceleration tube length of around 2 m, the length of the portion of the test gas in the shock tube from which the test flow originates is around a factor of 10 smaller than the values shown in Table II for a 25 m acceleration tube. Nevertheless, even in the case of a 2 m acceleration tube, the nonequilibrium post-shock region in the conditions apart from condition 1 correspond to no more than 15% of the portion of the test gas in the shock tube from which the test flow originates. Therefore, the nonequilibrium post-shock region is still unimportant in conditions other than condition 1 in small-scale facilities.

B. Pre-expansion post-shock nonequilibrium (conditions 7–12)

The results for conditions 7–12 are presented in this section. The low pressure in the shock tube for these conditions means that the post-shock relaxation distance is large. Therefore, the nonequilibrium post-shock portion of the test gas could contribute to a significant portion of the test flow. As a result, this is modeled in the simulations for these conditions, and an opportunity is presented to investigate the combined post-shock nonequilibrium and unsteady expansion nonequilibrium.

The nonequilibrium post-shock flow is calculated via the space-marching code POSHAX[32] with Park's 2T model and used as the initial condition for the test gas in the L1d simulations. The discretization used for these simulations is the same as that used for the simulations presented in Sec. III A—200 and 5000 cells are used for the test gas and accelerator gas slugs, respectively—except the degree of clustering is different. The clustering of the cells for the test gas is made such that at least 50 cells are used to resolve the nonequilibrium post-shock region. For conditions 7 and 8, it was found that the same degree of clustering used for the simulation of conditions 1–6 in Sec. III A is enough to resolve the post-shock nonequilibrium as shown in Fig. 21. Thus, simulations of conditions 7 and 8 are performed using this same setup (minimum cell length of 3 μm). However, for conditions 9–12, a stronger cluster is needed, corresponding to a minimum cell length of 1.7 and 1.2 μm for conditions 9 and 10 and conditions 11 and 12, respectively. Confirmation of adequate convergence of both spatial and temporal discretization is made by testing with a finer mesh (2× nominal) and with a smaller CFL number (0.25); the result for condition 11, which is the condition with the largest gradients in flow properties, is shown in Fig. 22 as an example.

1. Low acceleration tube fill pressure (conditions 7, 9, and 11)

The results for condition 7 are shown in Fig. 23(a). The nonequilibrium post-shock origin of the test flow is obvious when examining

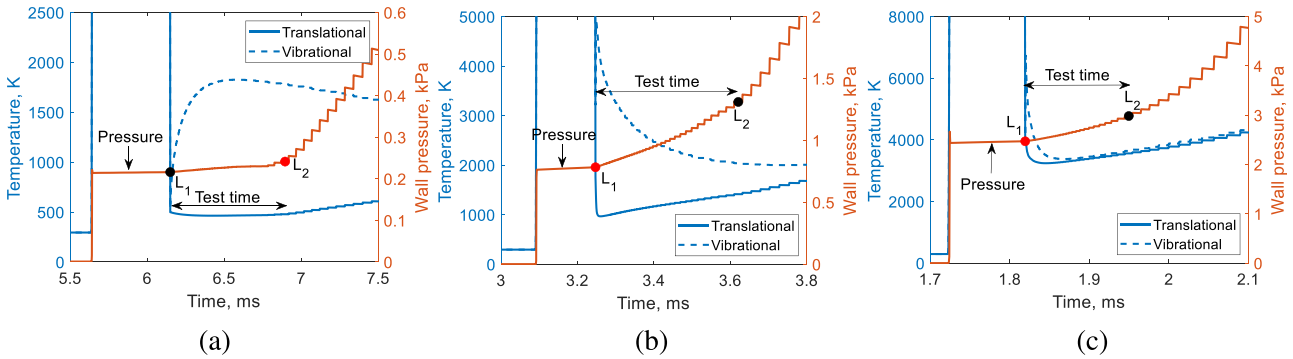

FIG. 23. Temperatures and static pressure for conditions (a) 7, (b) 9, and (c) 11. All at 25 m in the acceleration tube.

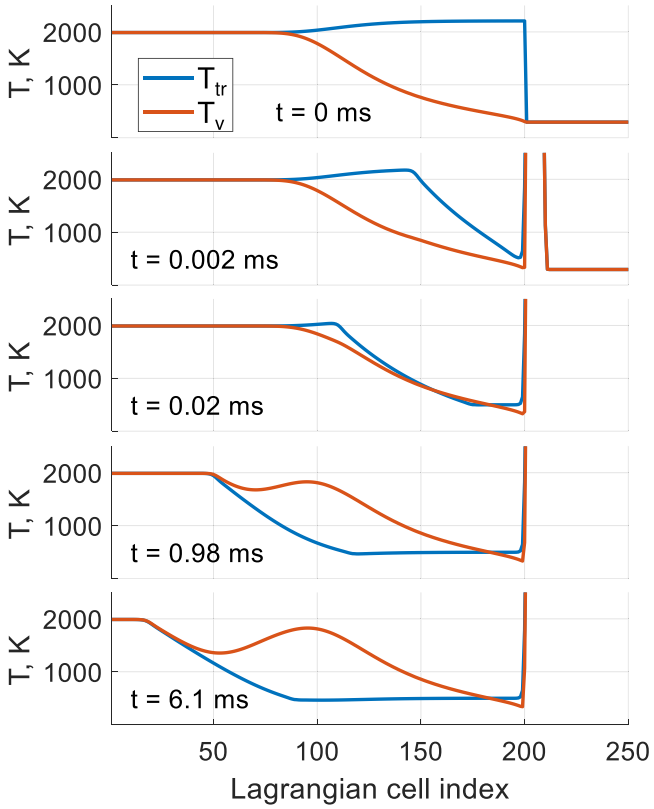

FIG. 24. Time evolution of the translational (T_{tr}) and vibrational (T_v) temperatures of the Lagrangian cells in condition 7. The test gas slug is represented by cells 1–200.

the vibrational nonequilibrium. Immediately after the contact surface, the test flow is actually equilibrated. The vibrational mode then rapidly increases and departs from equilibrium. The flow immediately after the contact surface originates from the flow immediately behind the shock front, which is essentially frozen with a very low vibrational temperature. The vibrational mode remains frozen through the expansion, and the translation temperature drops coincidently to values close to the vibrational temperature. Thus, in this case, equilibrium is achieved, not via the conventional mechanism of translational-vibrational energy transfer, but via manipulation of the translation temperature to match the vibrational temperature, which remains frozen. This is illustrated in Fig. 24, which shows the evolution of the temperatures of the Lagrangian cells with time; the vibrational temperature of the Lagrangian cells near the contact surface (cells 170–200), which forms the initial part of the test flow originating from the nonequilibrium post-shock region, remains frozen, while the translation temperature drops to values close to their vibrational temperature. The vibrational temperature of cells 100–170, which approximately makes up the rest of the test flow originating from the nonequilibrium post-shock region, remains frozen too. At the instance of $t = 0.02$ ms, the unsteady expansion fan causes a translation temperature profile that, by chance, nearly matches the vibrational temperature profile. However, beyond $t = 0.02$ ms, the translation temperature continues to decrease and eventually drops to values much lower than the vibrational temperature in cells 100–170, resulting in a nonequilibrium test flow.

The results for condition 9 are shown in Figs. 23(b) and 25(a), and, for condition 11, in Figs. 23(c) and 25(b). It can be immediately seen in these figures that, unlike in condition 7, the nonequilibrium post-shock part corresponds to only a small portion of the test flow—<10 μs and <1.2 μs in conditions 9 and 11, respectively—which is so small that it can be considered negligible for practical intents and purposes. The nonequilibrium feature of the test flow in conditions 9 and 11 is dominated by the nonequilibrium from the unsteady expansion and the results are, thus, somewhat similar to conditions 3 and 5, respectively, which are the higher shock tube fill pressure counterparts.

The shock and contact surface speeds are shown in Fig. 26 along with the theoretical frozen and equilibrium limits. Because the method of calculating the theoretical limits is a point-to-point framework, and a nonuniform initial condition exists in the test gas, the theoretical limits calculated would, thus, depend on which point in the nonuniform initial test gas condition is used as the pre-expansion condition. In this work, the condition at both ends of the initial test gas slug is used to calculate the theoretical limits. The condition at the upstream end (referred to as "back") is the equilibrium post-shock condition, and the condition at the downstream end (referred to as "front") is the frozen post-shock condition.

Looking at the shock and contact surface speeds for condition 7, shown in Fig. 26(a), the speeds are initially near the frozen limit, assuming a frozen post-shock condition for the pre-expansion

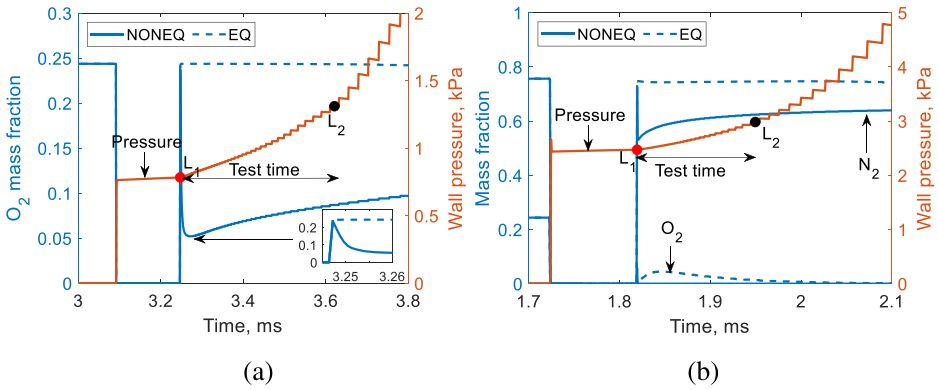

FIG. 25. Mass fractions and static pressure for conditions (a) 9 and (b) 11. All at 25 m in the acceleration tube.

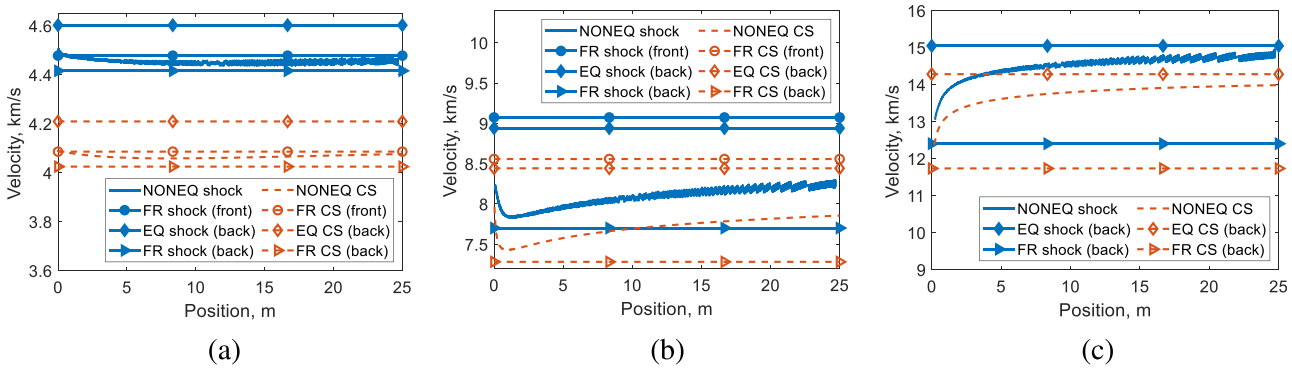

FIG. 26. NONEQ shock speed and CS profile along with the FR limits assuming a frozen post-shock condition for the pre-expansion condition (FR front) and an equilibrium post-shock condition for the pre-expansion condition (FR back), and the EQ limits assuming an equilibrium post-shock condition for the pre-expansion condition (EQ back) for test conditions (a) 7, (b) 9, and (c) 11.

condition (FR front), and then, it decelerates toward the frozen limit assuming an equilibrium post-shock condition for the pre-expansion condition (FR back) as the expansion fan propagates through the significantly large post-shock nonequilibrium region. Beyond about 15 m, the shock and contact surface then accelerate toward the equilibrium limit. However, the acceleration is very gradual, and the speeds are still near the frozen limits by 25 m. This lack of equilibration is unsurprising for condition 7, which corresponds to the lower bound of the shock tube fill pressure and the lower bound of the acceleration tube fill pressure. In condition 9, as mentioned earlier, the nonequilibrium post-shock part corresponds to only a small portion of the test flow, and this is further reflected in the shock and contact surface speeds in Fig. 26(b). Only over the first meter do the speeds manifest the influence of the post-shock nonequilibrium region—the deceleration between the two frozen limits. Beyond 1 m, the speeds accelerate toward the equilibrium limit but do not reach this limit within 25 m. In condition 11, the nonequilibrium post-shock part corresponds to a negligible portion of the test flow, and the main nonequilibrium feature is dominated by the nonequilibrium from the unsteady expansion propagating into an equilibrium post-shock state as mentioned earlier. This is further evident in the shock and contact surface speeds in Fig. 26(c), where the speeds are seen to only accelerate from near the frozen limit toward the equilibrium limit without reaching the equilibrium limit within 25 m. Condition 11 also demonstrates the earlier finding that the shock speed may not be a reliable indicator for the degree of thermochemical nonequilibrium in the test flow; at 25 m downstream in the acceleration tube, the shock speed is relatively near the equilibrium value as shown in Fig. 26(c), but the test flow contains appreciable nonequilibrium in the N_2 mass fraction as shown in Fig. 25(b).

2. High acceleration tube fill pressure (conditions 8, 10, and 12)

When the pre-expansion condition in conditions 7, 9, and 11 is expanded into an acceleration tube filled at 100 Pa instead of 1 Pa, an essentially equilibrium condition is observed as shown in Figs. 27 and 28, which correspond to the results for conditions 8, 10, and 12. There exists a very short unsteady portion immediately after the contact surface, which originates from the nonequilibrium post-shock portion of the pre-expansion condition; despite equilibration in this unsteady portion of the test flow, the flow properties, except the static pressure, are unsteady here because there is a dependency on the flow history. Beyond this brief period of unsteady flow, a steady flow is attained. For condition 8, this brief period of unsteady flow lasts for about 70 μs, which is only ≈3% of the total test time. For conditions 10 and 12, this period reduces to less than 5 μs and can be considered negligible for practical intents and purposes.

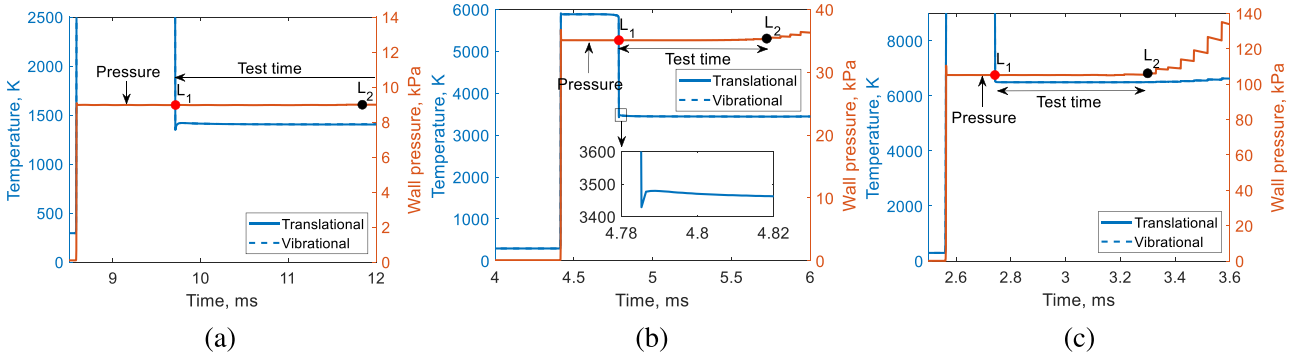

FIG. 27. Temperatures and static pressure for conditions (a) 8, (b) 10, and (c) 12. All at 25 m in the acceleration tube.

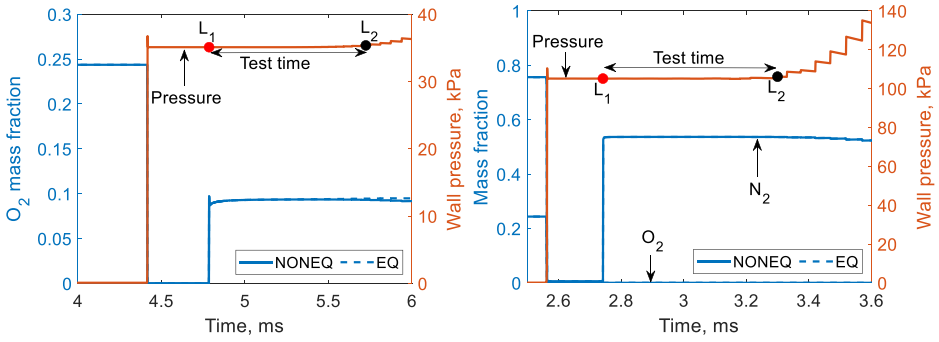

FIG. 28. Mass fractions and static pressure for conditions (a) 10 and (b) 12. All at 25 m in the acceleration tube.

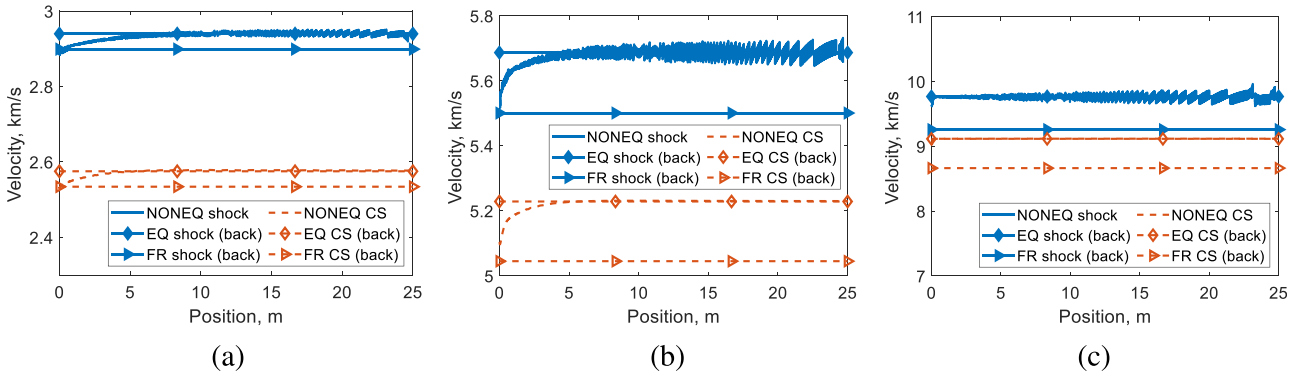

FIG. 29. NONEQ shock speed and CS profile along with the FR limits assuming an equilibrium post-shock condition for the pre-expansion condition (FR back), and the EQ limits assuming an equilibrium post-shock condition for the pre-expansion condition (EQ back) for test conditions (a) 8, (b) 10, and (c) 12.

For conditions 8, 10, and 12, the static pressure is steady throughout as shown in Fig. 27, and this is reflected in the shock and contact surface speeds in Fig. 29, which shows that the speeds at 25 m have a steady value close to the equilibrium limit. For conditions 8 and 10, the speeds begin near the frozen limit and then quickly accelerate toward the equilibrium limit. The equilibrium limit is reached after about 10 m and 5 m in conditions 8 and 10, respectively. In condition 12, the speeds reach the equilibrium limit much earlier and are essentially at the equilibrium limit throughout the length of the acceleration tube. This finding is consistent with earlier observations that the higher enthalpy test conditions are closer to equilibrium.

However, the degree of equilibration in the test flow of condition 8 may seem somewhat counter-intuitive, given the result of condition 2. In both conditions, the acceleration tube fill pressure is 100 Pa. The difference between the two conditions is the shock tube fill pressure—100 kPa in condition 2 and 1 kPa in condition 8. Yet, despite having a higher pressure, condition 2 contains more nonequilibrium than condition 8. To make sense of this observation, Fig. 30 is made comparing L_2 in condition 2 with L_2 in condition 8. As can be seen in the figure, a larger degree of expansion is seen in condition 2 where the decrease in temperature and pressure is larger than that in condition 8. This is due to the higher shock tube fill pressure in condition 2, while the acceleration tube fill pressure remains unchanged. Although the pressure in condition 2 is higher than the pressure in condition 8 throughout, condition 2 is expanded to a much lower translational temperature, and maintaining equilibrium is difficult at such low temperatures. Therefore, deviation from equilibrium can be observed below 1000 K in condition 2. On the other hand, for condition 8, the translational temperature never drops below 1400 K, and equilibrium is, therefore, maintained.

3. Significance of the post-shock nonequilibrium region

To quantify the contribution of the nonequilibrium post-shock region in the test flow for conditions 7–12, an analysis of the

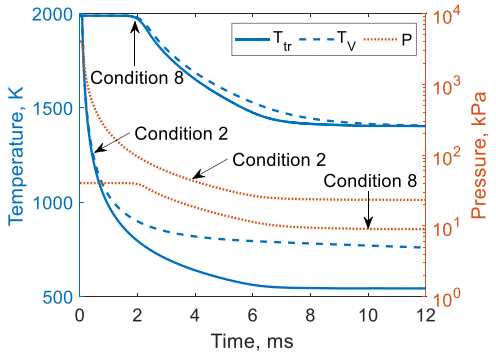

FIG. 30. Temperatures and static pressure history of Lagrangian cell L_2 in conditions 2 and 8.

TABLE III. The post-shock relaxation distance of the shock in the shock tube, and the length of the portion of the test gas in the shock tube corresponding to the test flow for conditions 7–12 for a 25 m acceleration tube.

Condition	7	8	9	10	11	12
Post-shock relaxation distance (m)	1×10^{-1}	1×10^{-1}	1×10^{-2}	1×10^{-2}	1×10^{-4}	1×10^{-4}
Portion of test gas in shock tube (m)	8×10^{-2}	2×10^{0}	6×10^{-2}	1×10^{0}	2×10^{-2}	1×10^{0}

Lagrangian cells is performed to determine the portion of the test gas in the shock tube corresponding to the test flow as done previously in Sec. III A 3 for conditions 1–6. The results are shown in Table III along with the post-shock relaxation distance extracted from Fig. 7(b). Earlier, it was suggested that because the post-shock relaxation distance is larger in conditions with lower shock tube fill pressures, a significant portion of the test flow may originate from the nonequilibrium post-shock region in many of the conditions in conditions 7–12. However, the results in Table III show that this is the case only in condition 7 for a 25 m acceleration tube. For a small-scale facility with an acceleration tube length of around 2 m, the nonequilibrium post-shock portion of the test gas would also be important in conditions 8 and 9 due to the linear relationship between the length of the acceleration tube and the length of the portion of the test gas in the shock tube from which the test flow originates from.

The rather lack of contribution from the nonequilibrium post-shock flow compared with what may be expected is because the lower shock tube fill pressure not only increases the post-shock relaxation distance but also increases the portion (length) of the test gas in the shock tube corresponding to the test flow. This can be observed by examining Tables II and III and comparing each low (1 Pa) acceleration tube fill pressure condition with its high (100 Pa) acceleration tube fill pressure counterpart (e.g., comparing condition 1 with condition 2; 3 with 4; 5 with 6; and so on). This trend for the length of the test gas in the shock tube is because conditions 7–12 undergo a weaker expansion compared to their counterparts in conditions 1–6. That is, the difference between the pre-expansion pressure and post-expansion pressure is smaller in conditions 7–12 compared with their higher shock tube fill pressure counterparts. As a result, the test gas slug undergoes less stretching in conditions 7–12, which means that a given length of test flow would originate from a larger portion (length) of the test gas in the shock tube.

In light of the results in Tables II and III, it can be suggested that, instead of just the shock tube fill pressure, the shock tube shock speed (total enthalpy) and acceleration tube fill pressure (or the difference between the shock tube and acceleration tube fill pressures) also need to be considered when predicting the degree of contribution of the nonequilibrium post-shock region in the test flow—the contribution of the nonequilibrium post-shock region is increased by decreasing the shock tube fill pressure, increasing the difference between the shock tube and acceleration tube fill pressures, and decreasing the shock tube shock speed, and vice versa.

TABLE IV. ET secondary diaphragm hold time for different primary shock speeds.

Primary shock speed (km/s)	1.5	2.0	3.5	5.2	7.0
Hold time (μs)	≈200	≈150	≈50	≈10	≈5
Reference	49	49	50	40	51

C. Non-ideal diaphragm ruptures (conditions 7*, 9*, and 11*)

Another aspect of the ET flow cycle that requires consideration is the possibility of a non-ideal secondary diaphragm rupture. Some studies show that the secondary diaphragm rupture is close to ideal,[45–47] while some demonstrate clear evidence of non-ideal ruptures.[42,48] The simulation results presented thus far only assume ideal diaphragm ruptures. Therefore, it is of interest to also assess the influence of non-ideal ruptures.

Modeling of the secondary diaphragm rupture in ETs is most commonly done using the holding-time diaphragm model where the diaphragm opens after a certain delay after the arrival of the incident shock.[48] Reported values for the hold time show dependency on primary shock speed as summarized in Table IV. The data fit well with a fifth-order polynomial as shown in Fig. 31. Using this fit for the hold time, conditions 7, 9, and 11 are simulated using the holding-time diaphragm model for the secondary diaphragm rupture; these conditions will be denoted with an asterisk (e.g., conditions 7*, 9*, and 11*).

For the simulation of conditions 7*, 9*, and 11*, the initial condition used is identical to that used for the simulation of their ideal diaphragm rupture counterparts. However, the mesh used is slightly different and is illustrated in Fig. 32 for condition 7* as an example. Like with the previous simulations, 200 and 5000 cells are used for the test gas and accelerator gas slugs, respectively, for the nominal simulation. However, slightly different clustering is designed for the test gas slug. As shown in Fig. 32, the test gas slug has two regions. Region 1 consists of 150 cells with mild clustering toward $x = 0$, resulting in a rather uniform discretization. This is done to accommodate for the

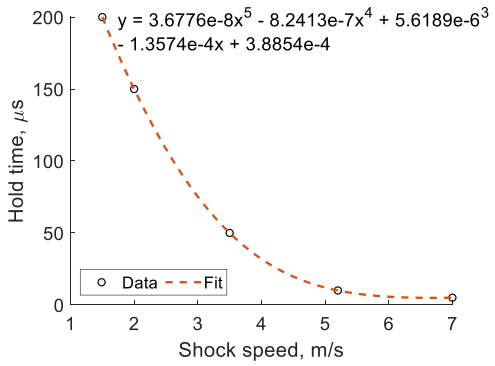

FIG. 31. Polynomial fit of the ET secondary diaphragm hold time for different primary shock speeds.

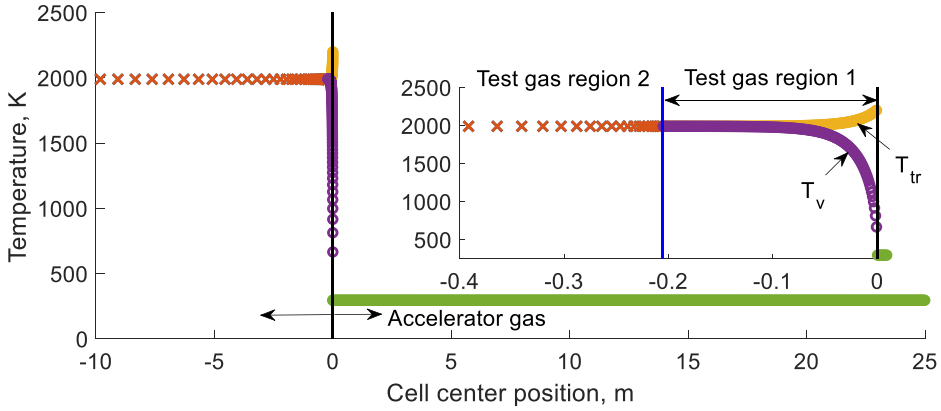

FIG. 32. Initial temperature distribution and cell center positions for condition 7∗. For clarity in the figure, only every second point is shown.

presence of a reflected shock due to the delayed opening of the diaphragm and to adequately resolve its post-shock relaxation. The cell spacing is also small enough to resolve the initial nonequilibrium post-shock region (from the incident shock). The length of region 1 is made such that the reflected shock is located not far from the boundary of regions 1 and 2 when it is caught by the expansion wave head. After this moment in time, the reflected shock will propagate through region 2 while it gets attenuated by the expansion fan. Due to this, as well as the fact that the cells in region 2 will undergo a slower and more gradual expansion, only 50 cells are used for region 2 in which stronger clustering toward the boundary with region 1 is made to ensure matching cell sizes across the boundary and achieve a gradual variation in cell size.

Mesh convergence is confirmed via simulation with a finer mesh containing twice as many cells and halved cell spacings as shown in Fig. 33 for conditions 7^*, 9^*, and 11^*. Overall, good agreement is observed between the fine and nominal results. For condition 9^*, there does exist an observable deviation in the spatial location of the shock and contact surface as shown in the zoomed-in view, which indicates some slight discrepancies in the shock speed and contact surface speed between the two simulations. However, these differences are found to be less than 0.5%, which is essentially negligible for practical intents and purposes.

The results from the finer mesh simulations are shown in Figs. 34 and 35. The test flow properties are unsteady, apart from the velocity and total enthalpy. Overall, conditions 7^*, 9^*, and 11^* resemble their respective ideal diaphragm rupture counterparts but with a larger amount of nonequilibrium. For condition 7^*, the vibrational temperature remains greater than 1800 K throughout the test time, while the vibrational temperature for condition 7 has a maximum value of only 1800 K in the test time. Also, for condition 7^*, the reflected shock causes mild O_2 dissociation to occur before the expansion. The O_2 mass fraction of the cells between L_1 and L_2 remains essentially frozen through the expansion and subsequent flow through the acceleration tube, as shown in Fig. 36(b), resulting in a test flow with mildly dissociated O_2. For condition 9^*, the vibrational temperature remains greater than 3500 K during the test time, while the vibrational temperature of condition 9 remains less than 3500 K during the majority of the test time.

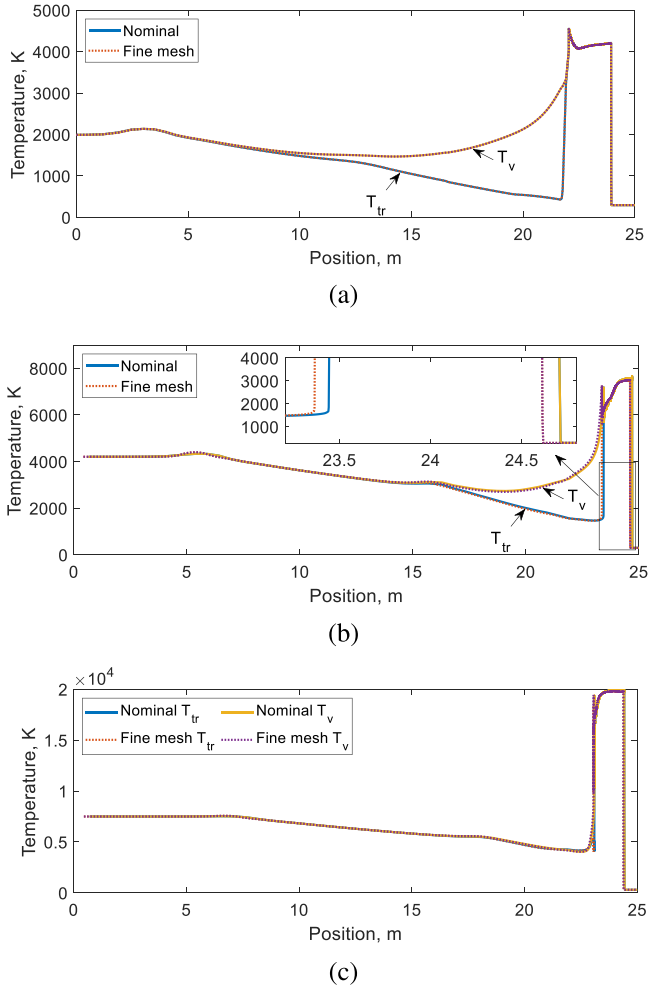

FIG. 33. Translational temperature distribution for (a) condition 7∗ at $t = 5.6$, (b) condition 9∗ at $t = 2.8$, and (c) condition 11∗ at $t = 1.6$ ms.

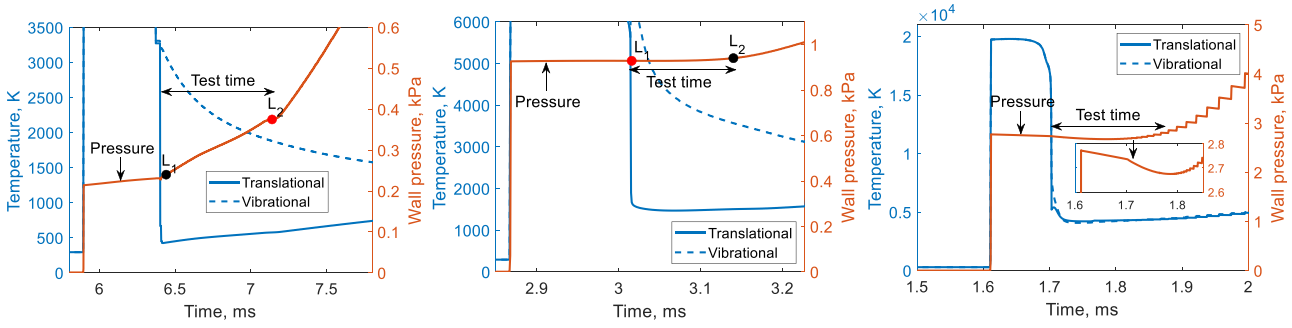

FIG. 34. Temperatures and static pressure for conditions (a) 7∗, (b) 9∗, and (c) 11∗. All at 25 m in the acceleration tube.

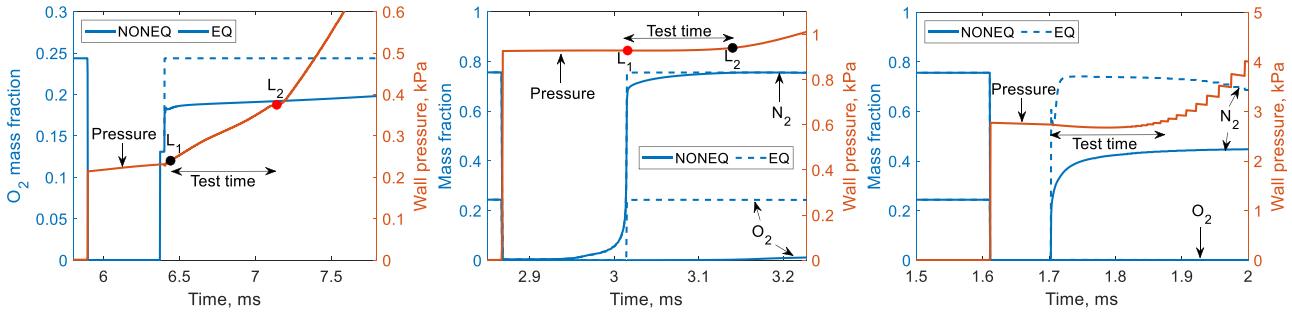

FIG. 35. Mass fractions and static pressure for conditions (a) 7∗, (b) 9∗, and (c) 11∗. All at 25 m in the acceleration tube.

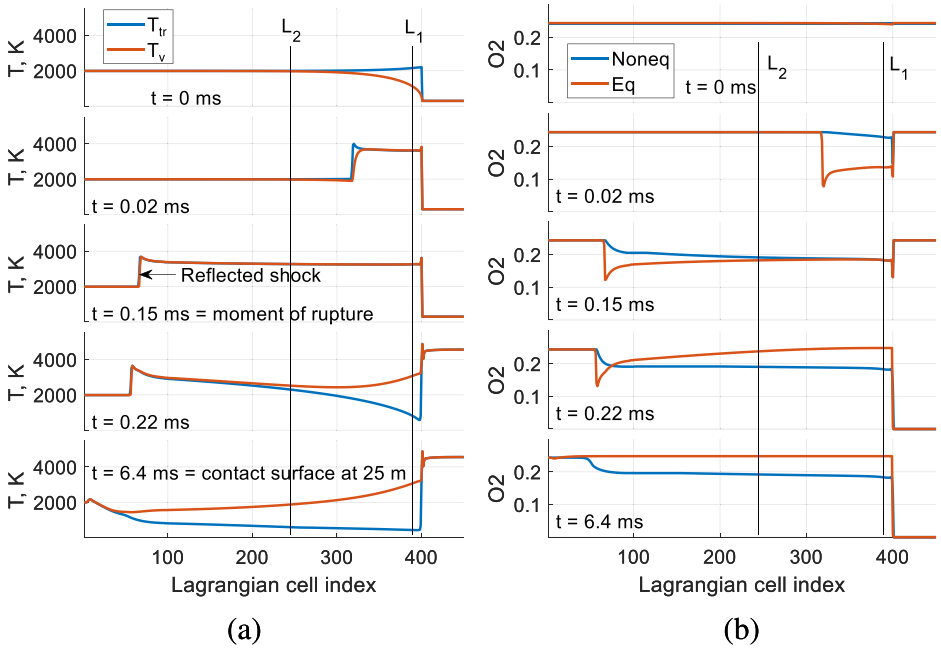

FIG. 36. Time evolution of the (a) temperatures and (b) O_2 mass fraction of the Lagrangian cells in condition 7∗. The test gas slug is represented by cells 1–400.

The O_2 mass fraction in condition 9* is essentially completely dissociated and frozen, whereas the O_2 mass fraction in condition 9 is only partially dissociated and shows some recombination during the test time. There is even some mild N_2 dissociation in condition 9* due to the higher pre-expansion temperature caused by the reflected shock from the delayed opening of the diaphragm. Unlike the O_2 mass fraction, the N_2 mass fraction in condition 9* does show some recombination during the test time, which eventually leads to full recombination by the end of the test time. Condition 11* resembles condition 11, which essentially has an equilibrated vibrational mode, an equilibrated O_2 mass fraction that is completely dissociated, and a nonequilibrium N_2 mass fraction. Though, a larger N_2 mass fraction nonequilibrium is seen in condition 11* compared with condition 11 due to the reflected shock from the diaphragm causing increased dissociation.

In conditions 7*, 9*, and 11*, thermochemical equilibrium is achieved after being processed by the reflected shock and before expansion for the slug of test gas making up the test flow (slug between L_1 and L_2) as shown exemplarily in Fig. 36 for condition 7*. As shown in the figure, the test gas at and downstream of L_2 (cells 240–400) is found to be processed by the reflected shock and in thermochemical equilibrium at the time of diaphragm rupture. As a result, the nonequilibrium trend for conditions 7*, 9*, and 11* is dominated by the nonequilibrium from the unsteady expansion and essentially has no indications of the nonequilibrium post-shock region. Beyond the moment of rupture, the unsteady expansion fan head chases the reflected shock and eventually catches it. After that, the expansion fan attenuates the reflected shock. By the time the contact surface reaches 25 m in the acceleration tube, the reflected shock is almost completely attenuated.

Figure 37 compares the shock and contact surface speeds in the acceleration tube with the frozen and equilibrium limits from the equilibrium condition behind the reflected shock (FR Refl. and EQ Refl., respectively), and the equilibrium limit from the equilibrium condition behind the incident shock (EQ Incdt.). As one would expect, the shock and contact surface accelerate from near the frozen limit toward the equilibrium limits. The shock speed is relatively near the equilibrium limits at 25 m downstream in the acceleration tube in conditions 9* and 11*. Since the test flows contain significant nonequilibrium at 25 m downstream in the acceleration tube as shown in Figs. 34 and 35, these two conditions further demonstrate the earlier finding that the shock speed may not be a reliable indicator for the degree of nonequilibrium in the test flow.

The shock and contact surface speeds in condition 7* never reach the equilibrium limits by 25 m and have a significant acceleration at 25 m. This acceleration is reflected in the static pressure of the test flow shown in Fig. 34(a), which increases significantly during the test time. For extremely large facilities where the length of the acceleration tube is much longer than 25 m, one would expect the secondary shock speed to eventually equal the equilibrium shock speed from the equilibrium condition behind the incident shock in the shock tube (EQ Incdt.). This is because the reflected shock would eventually attenuate completely and the expansion fan would propagate entirely in a gas mixture originating from the equilibrium condition behind the incident shock. However, the secondary shock speed may temporarily overshoot this limiting speed before reaching this limit as shown in Figs. 37(b) and 37(c) for conditions 9* and 11*, respectively.

In conditions 9* and 11*, the shock and contact surface speeds initially accelerate from near the frozen limit toward the equilibrium limits. The magnitude of acceleration decreases as the shock and contact surface travel downstream in the acceleration tube. By around 18 m and 5 m in conditions 9* and 11*, respectively, the shock and contact surface are traveling at an almost constant speed not equal to "EQ Incdt." This speed is above EQ Incdt. but below the equilibrium limit from the equilibrium condition behind the reflected shock (EQ

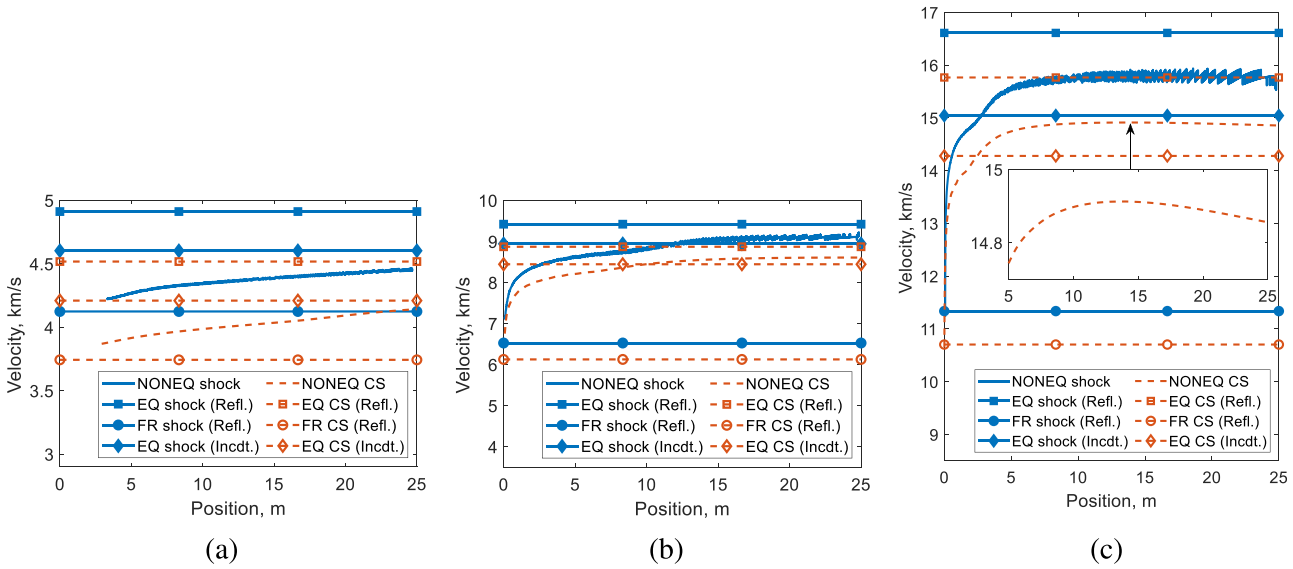

FIG. 37. NONEQ shock speed and CS profile along with the FR limits assuming an equilibrium reflected shock condition for the pre-expansion condition (FR Refl.), the EQ limits assuming an equilibrium reflected shock condition for the pre-expansion condition (EQ Refl.), and the EQ limits assuming an equilibrium incident shock condition for the pre-expansion condition (EQ Incdt.), for conditions (a) 7∗, (b) 9∗, and (c) 11∗.

Refl.). This pseudo-asymptotic behavior is due to competition between two processes—thermochemical relaxation and attenuation of the reflected shock. These are two competing processes because the former increases the shock and contact surface speeds as discussed earlier, while the latter decreases the shock and contact surface speeds, as shown in Fig. 37, where "EQ Refl." is higher than EQ Incdt. Beyond 25 m (in even larger facilities) for condition 9*, a slight deceleration of the shock and contact surface speeds would eventually have to occur due to the overshoot of the limiting speed EQ Incdt. For condition 11*, this slight deceleration can already be observed within 25 m. Zooming in, it can be seen in Fig. 37(c) that the contact surface actually has a mild deceleration after 15 m.

As a result of the relatively steady shock and contact surface speeds, the static pressure remains rather steady throughout the test time in conditions 9* and 11* at 25 m despite the existence of significant nonequilibrium in the test flow. In condition 11*, a mild decrease in static pressure is observed in Fig. 34(c) to correspond with the mild deceleration of the shock and contact surface at 25 m in Fig. 37(c). Condition 11* is the only condition shown in this paper to feature a negative rate of change in static pressure during the test time and, correspondingly, a decelerating shock wave/contact surface at 25 m.

IV. IMPLICATIONS OF THE RESULTS

A. Postulating the combined effects of viscosity and thermochemical nonequilibrium

The current work shows that, in general, thermochemical nonequilibrium accelerates the secondary shock speed from the frozen limit toward the equilibrium limit. Viscosity and heat loss have the opposite effect of decelerating the shock speed.[14,41] Therefore, in a real ET, the secondary shock speed is subjected to competition between the viscous and thermochemical nonequilibrium effects. Most existing experimental measurements indicate a decelerating secondary shock, which means that the viscous effect dominates.[41] Nevertheless, measurements of accelerating secondary shocks have also been reported.[49] In Ref. 41, two-dimensional viscous simulations assuming thermochemical equilibrium yielded shock speeds, static pressures, and pitot pressures, which cannot all be simultaneously reconciled with the corresponding experimental measurements, for both small- and large-scale ETs. The results from the current work indicate that thermochemical nonequilibrium in the unsteady expansion should be considered in ET modeling in order to predict the correct flow properties. On the other hand, the thermochemical nonequilibrium region behind the primary shock may be considered negligible for practical intents and purposes in most cases.

The steadiness of ET test conditions is another important aspect that needs to be considered. From Ref. 4 and the current results, viscosity and thermochemical nonequilibrium both cause a rate of change in the various flow properties during the test time. The current results show that thermochemical relaxation can be seen during the test time due to nonequilibrium; time-resolved measurements of the shock standoff distance, which decreases as the freestream equilibrates,[52] support this finding.[53] This relaxation produces a gradient in the translational and vibrational temperatures, mass fractions, and static pressure, while the velocity and total enthalpy remain essentially constant. Reference 4, assuming thermochemical equilibrium, showed that the interaction of the unsteady expansion of the test gas with the boundary layer causes a phenomenon that the authors call "test gas necking." Test gas necking is manifested most significantly in the static pressure of the test condition, as shown in Fig. 38 for the X3 ET, where a significant dip exists after the contact surface and before the arrival of the unsteady expansion fan. Because nonequilibrium produces a positive static pressure gradient in most cases, the negative gradient part of the dip would be somewhat offset when combining the effects of viscosity and nonequilibrium. However, the positive gradient part of the dip would have its gradient further increased by nonequilibrium. This could explain the characteristic shape of the experimental static (wall) pressure traces, measured in many ET test conditions, which contain a large positive pressure gradient without much of a dip like that seen in Fig. 38, which assumes equilibrium flow.[43,53,54]

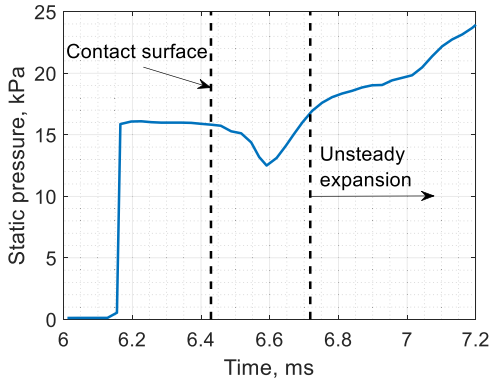

FIG. 38. Simulated test flow static pressure in the X3 ET (a large-scale facility) assuming equilibrium. Adapted from Ref. 4.

Test gas necking has a more minor influence on the flow velocity. Since thermochemical nonequilibrium also has only a small influence on the velocity, one would then expect the velocity to be one of the steadiest flow parameters of ET test conditions; recent experimental measurements of the velocity in an ET supports this conclusion.[55] This, consequently, means that the total enthalpy of ET test conditions, which is usually dominated by the kinetic energy component, should also be one of the steadiest flow parameters. This is supported by time-resolved measurements of the radiation emission near the stagnation point, which is governed mainly by the total enthalpy of the test condition,[56] showing a relatively constant value during the test time as reported numerously.[53,54,57]

B. On generating equilibrium and flight test conditions

As hinted at by earlier studies at selected conditions,[5,6,9,12,13] the current work comprehensively confirms that the test conditions generated in ETs can often contain significant nonequilibrium. Hence, from the trends observed in Sec. III, it is now important to present a discussion on generating equilibrium and flight test conditions in this facility. Regarding the creation of thermochemical equilibrium test conditions, the results show that a high acceleration tube fill pressure is crucial for achieving this by reducing the strength of the unsteady expansion. Although not explicitly shown in the current work, one may also expect a high shock tube fill pressure to help with equilibration. However, it is important that a high shock tube fill pressure is accompanied by a high acceleration tube fill pressure; otherwise, the

unsteady expansion may be too strong to allow thermochemical equilibrium in the test flow as discussed in Sec. III B 2. Thermochemical equilibrium is achieved in most of the high acceleration tube fill pressure conditions (conditions 6, 8, 10, and 12) at 25 m downstream in the acceleration tube. Having a larger facility (long acceleration tube) can also help with equilibration as the flow is given more time for thermochemical relaxation. The current results show that, for most conditions, most of the thermochemical relaxation occurs inside the unsteady expansion fan and the flow after the expansion remains almost frozen—this is consistent with the results in Refs. 5 and 6. Increasing the total enthalpy of the test condition by driving a stronger incident shock through the shock tube helps with equilibration as well because the higher temperature and pressure involved in the higher enthalpy conditions promote equilibration and outweigh the higher velocities (shorter time scales) involved in these conditions, which promote thermochemical freezing as shown in Sec. III A 2. Using a secondary diaphragm that is as thin/light as practically possible will further help with equilibration by avoiding the generation of a reflected shock, which is shown in Sec. III C to increase the amount of nonequilibrium in the test flow.

The generation of flight replicating test conditions is a separate discussion. From earlier studies,[52,56,58–60] to appropriately replicate flight, the test condition needs to be in thermochemical equilibrium and have the correct temperature, pressure, and velocity, which are the freestream parameters at some point on the flight trajectory of a flight vehicle. According to the various Earth atmosphere models, the flight temperature will always be below 300 K. The issue with generating thermochemical equilibrium conditions with such temperatures (<300 K) has long troubled the community. For most of the high acceleration tube fill pressure conditions tested in the current work (the even-numbered conditions), the test flow is in thermochemical equilibrium in a large-scale facility but the temperature is around 500–6000 K, which is significantly higher than in flight. For the low acceleration tube fill pressure conditions tested in the current work (the odd-numbered conditions), the test flow is in nonequilibrium even in a large-scale facility and the temperature is around 200–3000 K, which is still mostly greater than in flight. Consequently, it may not be possible, in general, to produce flight-replicating test conditions in the ET. Nevertheless, this facility remains vital for fundamental studies and validation of general models for high enthalpy flows.

V. UNCERTAINTY FROM THE NONEQUILIBRIUM MODEL

In general, the quantitative result from any thermochemical nonequilibrium simulation depends on the type of thermochemical nonequilibrium model used as well as on the values of the finite rates used in the model. Various models and rates exist, but, due to the lack of appropriate experimental data, it is still rather unclear which of these existing models and rates are accurate, if any.[61] Even the high-fidelity state-to-state (StS) models, in which each molecular vibrational state is considered a pseudo-species, have significant uncertainties due to the uncertainties in the state-specific rates used, which can differ by orders of magnitude between different sources.[62] Thus, accurate modeling of thermochemical nonequilibrium remains an open problem and is very much an active area of research.[63]

In the current work, Park's 2T model[18] with five species is used to describe the thermochemical nonequilibrium as detailed in Sec. II A. In Ref. 56, it was shown that conditions that are close to the frozen or equilibrium limits are less sensitive to the thermochemical nonequilibrium model used. Thermochemical equilibrium is observed in many of the high acceleration tube fill pressure conditions simulated in the current work (conditions 6, 8, 10, and 12). The results of these conditions would, thus, be rather independent of the nonequilibrium model used. However, for the nonequilibrium conditions simulated in the current work, the results are expected to more or less change when different models and rates are used. Therefore, the focus of this paper has been on extracting more qualitative yet important trends, which may likely be valid universally (in real ETs and in simulations using other models and rates). This is possible as one can always find a set of initial (fill) conditions that would produce nonequilibrium flow in the facility, resulting in the reproduction of these trends. Strongly supporting this is the fact that numerous independent works have reported results that are consistent with the different trends found in the current work as discussed in Sec. IV. Nevertheless, it is still of interest to provide a basic understanding of how the results can quantitatively change with different models and rates.

To do this, zero-dimensional constant volume reactor simulations are conducted for the three initial conditions shown in Table V, which correspond to the equilibrium pre-expansion conditions in conditions 7–12 from shock speeds of 2, 4, and 7 km/s. For all three conditions, the translational temperature is instantaneously decreased to 700 K, and the resulting constant volume reactor is simulated to give a zero-dimensional analogy for the 1D unsteady expansion. In addition to Park's nominal 2T model, three other thermochemical nonequilibrium configurations are used here; the results are shown in Figs. 39 and 40.

There is empirical evidence that the N_2 vibrational relaxation time, $\tau_{v,N2}$, in expanding flows is up to 70 times faster than its corresponding value under post-shock conditions.[64] Therefore, the $\tau_{v,N2}$ used in Park's 2T model, which is derived for post-shock conditions, is reduced by a factor of 70, resulting in the "2T fast" model. For the rate controlling temperature, $T_c = T_{tr}^{0.5} T_v^{0.5}$, of the dissociation/recombination reactions, a popular alternative is $T_c = T_{tr}^{0.7} T_v^{0.3}$.[65] The "2T mod." model uses this modified T_c. In addition to these variations of the 2T model, the five species vibrational StS model described in detail in Refs. 44, 56, and 62 is tested. In this StS model, there are 61 bound vibrational levels for N_2, 46 for O_2, and 48 for NO, all obtained from the STELLAR database.[66] Only the ground electronic state is considered for all species, and equilibration between translational and rotational modes is assumed. Along with the thermal energy exchange reactions involving the vibrational and translational modes, the N_2, O_2, and NO dissociation/recombination reactions and the two

TABLE V. Initial conditions in a constant volume reactor.

Condition	I	II	III
Pressure (kPa)	40	200	500
Temperature (K)	2000	4000	7500
N_2 and O_2 mass fractions	c_{N2}:0.76, c_{O2}:0.24	c_{N2}:0.72, c_{O2}:0.06	c_{N2}:0.45, c_{O2}:0.00

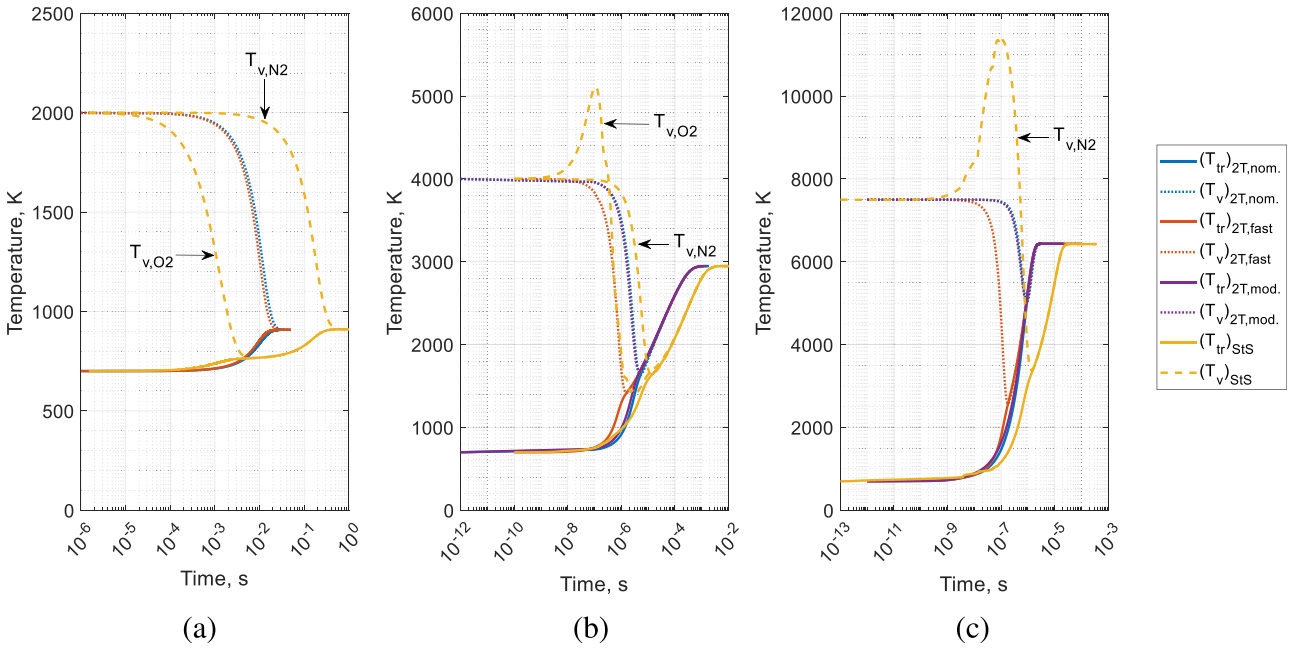

FIG. 39. Temperatures of the constant volume reactor for conditions (a) I, (b) II, and (c) III.

Zel'dovich reactions are modeled. The state-specific rates used originate from a combination of Forced Harmonic Oscillator (FHO) theory,[67] quasi-classical trajectory (QCT) calculations,[68] and the classic Landau–Teller (LT) model in StS form.[69]

As mentioned earlier, in general, no definitive conclusions can be made regarding the accuracy of these thermochemical nonequilibrium configurations at present. Thus, we will examine the results and discuss only the differences between these different configurations without suggesting which one is better than the others. From the vibrational nonequilibrium shown in Fig. 39, one can see that, apart from the modified 2T model, which is essentially identical to the nominal 2T model, the different configurations can produce different results. While the difference between the fast 2T model and nominal 2T model is small for condition I as shown in Fig. 39(a), this difference increases with increasing total enthalpy; for condition III, as shown in Fig. 39(c), thermal equilibrium in the fast 2T model is achieved an order of magnitude earlier. In the 2T models, the vibrational modes are assumed to be tightly coupled among the molecules where they are described by a single vibrational temperature. However, the StS model here indicates that the species have different vibrational temperatures; O_2 equilibrates significantly faster than N_2. Nevertheless, consistent with the findings in Refs. 56 and 58, the single vibrational temperature of the nominal 2T model lies between the O_2 and N_2 vibrational temperatures of the StS model; this can be observed in Figs. 39(a) and 39(b) after the overshoot in $T_{v,O2}$ caused by the O_2 recombination. The O_2 vibrational temperature is not shown in Fig. 39(c) because the mass fraction of O_2 is less than 10^{-3} throughout. Overall, the vibrational temperature among the different models at any given time can differ by up to around 1000, 1500, and 4000 K, in conditions I–III, respectively. The mass fractions, on the other hand, are less sensitive to changes in the thermochemical nonequilibrium configurations as shown in Fig. 40. One can see that all the 2T variants produce essentially the same results, which does, however, differ from the StS result; consistent with the earlier finding in Refs. 56 and 70, the current results show that the 2T model computes faster chemical recombination. Between the StS and 2T mass fraction results, the difference at any given time can be up to around 0.05 for O_2 in condition II and 0.1 for N_2 in condition III.

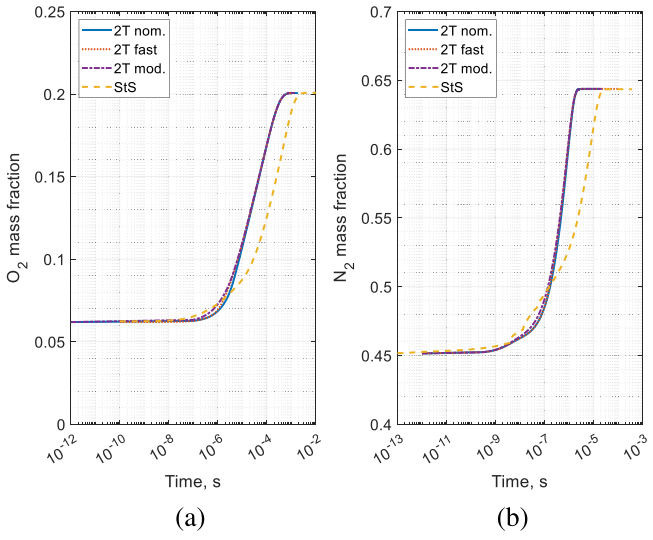

FIG. 40. (a) O_2 mass fraction in condition II and (b) N_2 mass fraction in condition III for the constant volume reactor.

Extending these overall results, it may be inferred that the thermal nonequilibrium results presented in Sec. III may have significant

quantitative changes in T_v if different thermochemical nonequilibrium configurations are used. On the other hand, the chemical nonequilibrium results are more certain, and the mass fractions should not change too much when different thermochemical nonequilibrium configurations are used. Finally, the results in this section support and enhance the reported difficulty with generating thermochemical equilibrium test conditions with low temperatures, discussed in Sec. IV B, because this has been demonstrated in this paper using even the 2T model, which is suggested by current and past results[56,70] to already give faster thermochemical relaxations.

VI. CONCLUSIONS

Using a 1D Lagrangian solver, thermochemical nonequilibrium simulations are performed for the entire range of practical operating conditions of ETs to isolate the influence of thermochemical nonequilibrium and identify key features in large-scale facilities. Particular attention is given not only to the nonequilibrium unsteady expansion but also to the influences of the thermochemical nonequilibrium region behind the primary shock and non-ideal secondary diaphragm rupture.

The nonequilibrium in the unsteady expansion is found to be the most influential process on the test flow—it can significantly influence the flow properties and cause significant temporal variations in the properties, except the velocity and total enthalpy, during the test time. The current results show that, for most conditions, most of the thermochemical relaxation occurs inside the unsteady expansion fan and the flow after the expansion remains almost frozen. Consequently, the shock speed may not be a reliable indicator for the degree of thermochemical nonequilibrium in the test flow as shown exemplarily in conditions 5, 11, 9*, and 11*. The nonequilibrium in the unsteady expansion is found to accelerate the shock and contact surface. This acceleration is caused by a pressure gradient. Due to the necessary condition that the static pressure and velocity across the contact surface are constant, the static pressure and velocity, unlike the temperatures and mass fractions, cannot retain information about the past. The non-ideal secondary diaphragm rupture is found to increase the amount of thermochemical nonequilibrium in the test flow due to the generation of a reflected shock. The attenuation of this reflected shock by the unsteady expansion fan causes a decelerating contribution to the secondary shock speed. In general, the diaphragm hold time is found to be long enough to allow the entire test flow to originate from the equilibrium condition behind the reflected shock. The thermochemical nonequilibrium region behind the incident primary shock may be considered negligible in most conditions.

Regarding the creation of thermochemical equilibrium test conditions, the results show that a high acceleration tube fill pressure is crucial for achieving this by reducing the strength of the unsteady expansion. Equilibrium is achieved in most of the high acceleration tube fill pressure conditions (conditions 6, 8, 10, and 12) at 25 m downstream in the acceleration tube. Having a larger facility (long acceleration tube) can also help with equilibration as the flow is given more time for thermochemical relaxation. Increasing the total enthalpy of the test condition by driving a stronger incident shock through the shock tube helps with equilibration as well, because the higher temperature and pressure involved in the higher enthalpy conditions promote equilibration and outweigh the higher velocities (shorter time scales) involved in these conditions, which promote thermochemical freezing.

Simulations of fixed-volume reactors at various de-excitation conditions performed using different thermochemical nonequilibrium models indicated that the vibrational temperature is quantitatively more sensitive and mass fractions is less sensitive to the modeling. Nevertheless, the more qualitative trends discussed in this paper may likely be valid universally, and supporting this is the fact that numerous independent works have reported consistent observations.

ACKNOWLEDGMENTS

This work was supported by the Hong Kong Research Grants Council (Grant No. 15206522).

AUTHOR DECLARATIONS

Conflict of Interest

The authors have no conflicts to disclose.

Author Contributions

Sangdi Gu: Conceptualization (lead); Formal analysis (lead); Funding acquisition (lead); Investigation (lead); Methodology (lead); Writing – original draft (lead); Writing – review & editing (lead). **Jiaao Hao:** Investigation (supporting); Supervision (equal); Writing – review & editing (supporting). **Qiu Wang:** Investigation (supporting); Supervision (supporting). **Chih-Yung Wen:** Investigation (supporting); Supervision (equal); Writing – review & editing (supporting).

DATA AVAILABILITY

The data that support the findings of this study are available within the article.

REFERENCES

[1]S. Gu and H. Olivier, "Capabilities and limitations of existing hypersonic facilities," Prog. Aerosp. Sci. **113**, 100607 (2020).
[2]C. Park, "Experimental aspects of nonequilibrium flow," in *Nonequilibrium Hypersonic Aerothermodynamics* (Wiley, New York, 1989), Chap. 7, pp. 219–254.
[3]A. Paull and R. Stalker, "Test flow disturbances in an expansion tube," J. Fluid Mech. **245**, 493–521 (1992).
[4]D. Gildfind, P. Jacobs, R. Morgan, W. Chan, and R. Gollan, "Scramjet test flow reconstruction for a large-scale expansion tube. II. Axisymmetric CFD analysis," Shock Waves **28**(4), 899–918 (2018).
[5]L. N. Connor, Jr., "Calculation of the centered one-dimensional unsteady expansion of a reacting gas mixture subject to vibrational and chemical nonequilibrium," NASA Technical Report No. TN D-3851, National Aeronautics and Space Administration, Langley Research Center, 1967.
[6]L. N. Connor, Jr., "The one-dimensional unsteady expansion of a reacting mixture of gases considering vibrational and chemical nonequilibrium," Ph.D. thesis (North Carolina State University, 1965).
[7]J. Ray *et al.*, "Estimation of inflow uncertainties in laminar hypersonic double-cone experiments," AIAA J. **58**(10), 4461–4474 (2020).
[8]A. Neely and R. Morgan, "The superorbital expansion tube concept, experiment and analysis," Aeronaut. J. **98**(973), 97–105 (1994).
[9]I. Nompelis, G. Candler, M. Holden, and T. Wadhams, "Numerical simulation of high-enthalpy experiments in the LENS X expansion tube facility," AIAA Paper No. 2004-1000, 2004.
[10]I. Nompelis, G. V. Candler, and M. S. Holden, "Effect of vibrational nonequilibrium on hypersonic double-cone experiments," AIAA J. **41**(11), 2162–2169 (2003).

[11]F. Liu and L. Bao, "Peak heat flux prediction of hypersonic flow over compression ramp under vibrationally excited free-stream condition," Phys. Fluids **35**, 016120 (2023).
[12]M. MacLean, A. Dufrene, T. Wadhams, and M. Holden, "Numerical and experimental characterization of high enthalpy flow in an expansion tunnel facility," AIAA Paper No. 2010-1562, 2010.
[13]P. Jacobs, T. Silvester, R. Morgan, M. Scott, R. Gollan, and T. McIntyre, "Superorbital expansion tube operation: Estimates of flow conditions via numerical simulation," AIAA Paper No. 2005-694, 2005.
[14]A. T. Dufrene, M. S. Holden, and M. J. Ringuette, "Microwave shock-speed diagnostic development and analysis of expansion tunnel viscous effects," AIAA J. **53**(3), 573–587 (2015).
[15]P. Jacobs, "Quasi-one-dimensional modeling of a free-piston shock tunnel," AIAA J. **32**(1), 137–145 (1994).
[16]P. A. Jacobs, "Shock tube modelling with L1d," Report No. 13/98, The University of Queensland, 1998.
[17]P. A. Jacobs, "Approximate Riemann solver for hypervelocity flows," AIAA J. **30**(10), 2558–2561 (1992).
[18]C. Park, "Review of chemical-kinetic problems of future NASA missions. I. Earth entries," J. Thermophys. Heat Transfer **7**(3), 385–398 (1993).
[19]J. W. Rich, S. O. Macheret, and I. V. Adamovich, "Aerothermodynamics of vibrationally nonequilibrium gases," Exp. Therm. Fluid Sci. **13**(1), 1–10 (1996).
[20]S. Gu, H. Olivier, C.-Y. Wen, J. Hao, and Q. Wang, "Characterization of reflected shock tunnel air conditions using a simple method," Phys. Fluids **34**(5), 056103 (2022).
[21]C. Mundt, R. Boyce, P. Jacobs, and K. Hannemann, "Validation study of numerical simulations by comparison to measurements in piston-driven shock-tunnels," Aerosp. Sci. Technol. **11**(2–3), 100–109 (2007).
[22]D. Gildfind, P. Jacobs, R. Morgan, W. Chan, and R. Gollan, "Scramjet test flow reconstruction for a large-scale expansion tube. I. Quasi-one-dimensional modelling," Shock Waves **28**(4), 877–897 (2018).
[23]J. Saavedra, G. Grossir, O. Chazot, and G. Paniagua, "Start-up analysis of a hypersonic short-duration facility," AIAA J. **60**(4), 2060–2074 (2022).
[24]G. Grossir, Z. Ilich, and O. Chazot, "Modeling of the VKI longshot gun tunnel compression process using a quasi-1D approach," AIAA Paper No. 2017-3985, 2017.
[25]R. Ramani, J. Reisner, and S. Shkoller, "A space-time smooth artificial viscosity method with wavelet noise indicator and shock collision scheme I. The 1-D case," J. Comput. Phys. **387**, 81–116 (2019).
[26]B. Grossman and P. Cinnella, "Flux-split algorithms for flows with non-equilibrium chemistry and vibrational relaxation," J. Comput. Phys. **88**(1), 131–168 (1990).
[27]R. Loubere and M. J. Shashkov, "A subcell remapping method on staggered polygonal grids for arbitrary-Lagrangian–Eulerian methods," J. Comput. Phys. **209**(1), 105–138 (2005).
[28]M. C. Cline, J. K. Dukowicz, and F. Addessio, "CAVEAT-GT: A general topology version of the caveat code," Technical Report No. LA-11812-MS, Los Alamos National Laboratory, 1990.
[29]M. Di Renzo, L. Fu, and J. Urzay, "HTR solver: An open-source exascale-oriented task-based multi-GPU high-order code for hypersonic aerothermodynamics," Comput. Phys. Commun. **255**, 107262 (2020).
[30]A. Peyvan, K. Shukla, J. Chan, and G. Karniadakis, "High-order methods for hypersonic flows with strong shocks and real chemistry," arXiv:2211.12635 (2022).
[31]L. Sciacovelli, D. Passiatore, P. Cinnella, and G. Pascazio, "Assessment of a high-order shock-capturing central-difference scheme for hypersonic turbulent flow simulations," Comput. Fluids **230**, 105134 (2021).
[32]D. F. Potter, "Modelling of radiating shock layers for atmospheric entry at Earth and Mars," Ph.D. thesis (University of Queensland, 2011).
[33]J. Shen, H. Lu, R. Li, X. Chen, and H. Ma, "The thermochemical non-equilibrium scale effects of the high enthalpy nozzle," Adv. Aerodyn. **2**(1), 1–20 (2020).
[34]Z. Jiang, J. Li, Z. Hu, Y. Liu, and H. Yu, "On theory and methods for advanced detonation-driven hypervelocity shock tunnels," Nat. Sci. Rev. **7**(7), 1198–1207 (2020).
[35]S. J. Stennett, D. Gildfind, P. Jacobs, R. Morgan, C. James, and P. Toniato, "The X3R free-piston reflected shock tunnel: Australia's new large-scale," AIAA Paper No. 2020-2447, 2020.
[36]D. E. Gildfind, R. G. Morgan, P. A. Jacobs, and M. McGilvray, "Production of high-Mach-number scramjet flow conditions in an expansion tube," AIAA J. **52**(1), 162–177 (2014).
[37]C. M. James, S. W. Lewis, R. G. Morgan, Y. Liu, and A. Lefevre, "Generating high-speed earth reentry test conditions in an expansion tube," J. Spacecr. Rockets **58**(2), 345–362 (2021).
[38]M. P. Scott, "Development and modelling of expansion tubes," Ph.D. thesis (University of Queensland, 2007).
[39]E. J. Fahy, "Superorbital re-entry shock layers: Flight and laboratory comparisons," Ph.D. thesis (University of Queensland, 2017).
[40]V. Wheatley, H. Chiu, P. A. Jacobs, M. N. Macrossan, D. J. Mee, and R. G. Morgan, "Rarefied, superorbital flows in an expansion tube," Int. J. Numer. Methods Heat Fluid Flow **14**(4), 512–537 (2004).
[41]D. E. Gildfind *et al.*, "Flow characterization and modeling of the X2 and X3 expansion tubes," NATO STO Lecture Series, STO-AVT-352-VKI, 2018.
[42]R. J. Bakos and R. G. Morgan, "Chemical recombination in an expansion tube," AIAA J. **32**(6), 1316–1319 (1994).
[43]C. James, D. Gildfind, S. Lewis, R. Morgan, and F. Zander, "Implementation of a state-to-state analytical framework for the calculation of expansion tube flow properties," Shock Waves **28**, 349–377 (2017).
[44]S. Gu, J. Hao, and C.-Y. Wen, "Air thermochemistry in the converging section of de Laval nozzles on hypersonic wind tunnels," AIP Adv. **12**(8), 085320 (2022).
[45]T. Furukawa, T. Aochi, and A. Sasoh, "Expansion tube operation with thin secondary diaphragm," AIAA J. **45**(1), 214–217 (2007).
[46]A. E. Nasser and J. W. Cleaver, "Vibrational relaxation of carbon monoxide in an unsteady expansion wave," Acta Astronaut. **4**(3–4), 357–373 (1977).
[47]V. A. Miller, M. Gamba, M. G. Mungal, and R. K. Hanson, "Secondary diaphragm thickness effects and improved pressure measurements in an expansion tube," AIAA J. **52**(2), 451–456 (2014).
[48]G. Wilson, "Time-dependent quasi-one-dimensional simulations of high enthalpy pulse facilities," AIAA Paper No. 1992-5096, 1992.
[49]S. Gu, "Mars entry afterbody radiative heating: An experimental study of non-equilibrium CO_2 expanding flow," Ph.D. thesis (University of Queensland, 2018).
[50]D. E. Gildfind, D. Smith, P. A. Jacobs, R. Kelly, A. Lefevre, and T. J. McIntyre, "Expansion tube test flow design for magnetohydrodynamic aerobraking," AIAA J. **59**(4), 1328–1341 (2021).
[51]R. Gollan *et al.*, "A simulation technique for radiating shock tube flows," in *26th International Symposium on Shock Waves, Göttingen, Germany*, edited by K. Hannemann and F. Seiler (Springer, Berlin, 2009), pp. 465–470.
[52]J. G. Hall and C. E. Treanor, "Nonequilibrium effects in supersonic-nozzle flows," AGARDograph No. 124, 1967.
[53]C. M. James *et al.*, "Improved test time evaluation in an expansion tube," Exp. Fluids **59**(87), 87 (2018).
[54]A. Sasoh, Y. Ohnishi, D. Ramjaun, K. Takayama, H. Otsu, and T. Abe, "Effective test time evaluation in high-enthalpy expansion tube," AIAA J. **39**(11), 2141–2147 (2001).
[55]T. Schwartz *et al.*, "Characterization of the Caltech hypervelocity expansion tube via tunable diode laser absorption spectroscopy," AIAA Paper No. 2021-3524, 2021.
[56]S. Gu, J. Hao, and C.-Y. Wen, "State-specific study of air in the expansion tunnel nozzle and test section," AIAA J. **60**(7), 4024–4038 (2022).
[57]C. James *et al.*, "Using optically filtered high-speed imaging to characterise expansion tube operating conditions," Shock Waves **30**(5), 523–544 (2020).
[58]C. Park, "Thermochemical relaxation in shock tunnels," J. Thermophys. Heat Transfer **20**(4), 689–698 (2006).
[59]C. Wen and H. Hornung, "Nonequilibrium recombination after a curved shock wave," Prog. Aerosp. Sci. **46**(2–3), 132–139 (2010).
[60]M. N. Macrossan, "Hypervelocity flow of dissociating nitrogen downstream of a blunt nose," J. Fluid Mech. **217**, 167–202 (1990).
[61]M. E. Holloway, R. S. Chaudhry, and I. D. Boyd, "Assessment of hypersonic double-cone experiments for validation of thermochemistry models," J. Spacecr. Rockets **59**(2), 389–400 (2022).
[62]S. Gu, J. Hao, and C.-Y. Wen, "On the vibrational state-specific modelling of radiating normal-shocks in air," AIAA J. **60**(6), 3760–3774 (2022).

[63]J. D. Schmisseur, "Hypersonics into the 21st century: A perspective on AFOSR-sponsored research in aerothermodynamics," Prog. Aerosp. Sci. **72**, 3–16 (2015).
[64]T. I. McLaren and J. P. Appleton, "Vibrational relaxation measurements of carbon monoxide in a shock-tube expansion wave," J. Chem. Phys. **53**(7), 2850–2857 (1970).
[65]G. V. Candler, "Nonequilibrium hypersonic flows and hypersonic nozzle flow modeling," NATO STO Lecture Series: Flow Characterization and Modeling of Hypersonic Wind Tunnels, STO-AVT-352-VKI, 2018.
[66]M. Lino da Silva, B. Lopez, V. Guerra, and J. Loureiro, "A multiquantum state-to-state model for the fundamental states of air: The stellar database," in *Proceedings of 5th International Workshop on Radiation of High Temperature Gases in Atmospheric Entry*, Barcelona, Spain, 16–19 October 2012, Vol. 714.
[67]I. V. Adamovich, S. O. Macheret, J. W. Rich, and C. E. Treanor, "Vibrational energy transfer rates using a forced harmonic oscillator model," J. Thermophys. Heat Transfer **12**(1), 57–65 (1998).
[68]F. Esposito and M. Capitelli, "The relaxation of vibrationally excited O_2 molecules by atomic oxygen," Chem. Phys. Lett. **443**(4–6), 222–226 (2007).
[69]W. Su, D. Bruno, and Y. Babou, "State-specific modeling of vibrational relaxation and nitric oxide formation in shock-heated air," J. Thermophys. Heat Transfer **32**(2), 337–352 (2018).
[70]J. Hao, J. Wang, and C. Lee, "State-specific simulation of oxygen vibrational excitation and dissociation behind a normal shock," Chem. Phys. Lett. **681**, 69–74 (2017).